WILEY | Hindawi

Research Article

Acceleration-Based Design Procedure for Sloped Rolling-Type Bearings with an Added Rotational Inerter

Yi-An Lai, Shiang-Jung Wang ⓘ, and Ting-Yu Hsu ⓘ

Department of Civil and Construction Engineering, National Taiwan University of Science and Technology, Taipei, Taiwan

Correspondence should be addressed to Ting-Yu Hsu; tyhsu@mail.ntust.edu.tw

This research numerically investigates the mechanical behavior of sloped rolling-type bearings equipped with an inerter. After deriving equations of motion, the mechanical behavior, under harmonic excitation, of a sloped rolling-type bearing with its inherent rotational mass (i.e., considering the inertial and restoring forces generated by the existing roller) and one with an added rotational inerter is numerically analyzed. It is demonstrated that the latter is mechanically different from the former and, more importantly, the latter is more effective at controlling acceleration and displacement responses and practically more feasible. The acceleration control performance designed for sloped rolling-type bearings that ignore the inherent rotational mass can basically be retained when adding a rotational inerter if a suitable inertance-to-mass ratio can first be determined based on a specific acceleration target. Precisely stated, retaining the unique mechanical feature of sloped rolling-type bearings under harmonic excitation (i.e., the maximum transmitted acceleration is irrelevant to the external disturbance) is the optimum design objective in this study. Parametric and numerical analyses show that the peak acceleration responses of sloped rolling-type bearings with an added rotational inerter whose inertance-to-mass ratio is determined based on the optimum objective are less dependent on having a sufficiently large harmonic excitation period (i.e., on having the roller in motion within the sloped rolling range). In addition, the peak displacement responses under harmonic excitation can be effectively reduced compared with sloped rolling-type bearings that only consider the inherent rotational mass (i.e., without an added rotational inerter). Similar tendencies are seen when the sloped rolling-type bearings are subjected to ground motion records including far-field and pulse-like near-fault ones. Regardless of the ground motion considered in this study, the sloped rolling-type bearings with an added rotational inerter designed based on the optimum objective show steady displacement reduction. Finally, a simple, practical, and acceleration-based procedure is proposed for designing sloped rolling-type bearings equipped with added rotational inerters based on observations from the parametric and numerical analyses.

1. Introduction

Sloped rolling-type bearings (SRBs) are constituted in each principle horizontal direction of cylindrical rollers sandwiched between upper and lower bearing plates, either or both of which are provided with a V-shaped rolling surface. SRBs designed with single sloping angles and friction damping forces, which feature constant horizontal acceleration control performance [1], have been numerically and experimentally demonstrated to be effective at seismically protecting critical equipment, facilities, and infrastructure [2–6]. The equations of motion for describing both the generalized and simplified horizontal transmitted acceleration of SRBs, however, were theoretically derived based on the assumption of negligible roller mass [4–6]. When the roller mass of an SRB is not negligible compared with the total mass of the protected object and upper bearing plate, it should be further analyzed even if this is not often seen in engineering practice. This is important if there is any potential adverse effect that could induce nonconservative design results. In addition, it has been found that SRBs designed with single sloping angles and friction damping forces do not perfectly control horizontal transmitted acceleration and isolation displacement simultaneously [7]. Accordingly, some strategies have been developed, such as SRBs being passively provided with linearly or stepwise

variable parameters [8, 9], as well as being improved in a semi-active manner [10, 11] and integrated with earthquake early warning information [12, 13].

Smith [14] first proposed a two-terminal inertial element, referred to as an inerter, based on the analogy between mechanical and electrical networks. It is synthesized using relatively lightweight components but can generate a remarkable level of positive-real impedance. By connecting the inerter with spring and dashpot elements in parallel, series, or hybrid configurations, significant negative stiffness, mass amplification, or period elongation effects can be achieved and thus act as a more effective energy dissipater or vibration absorber. Since it is a two-terminal inertial element, the reaction force generated by the movement of the inerter is approximately proportional to the relative acceleration between the two terminals. The proportionality constant is dubbed inertance or apparent mass, which is often designed to be much larger than the physical inerter mass (e.g., hundreds or thousands times greater). By expressing the generated force in the frequency domain, the property of negative stiffness can be easily understood. This idea can be practically realized by various physical mechanisms, such as the common rack-pinion [15], ball-screw [16], and hydraulic (or fluid) mechanisms [17].

Owing to the distinct advantages of the inerter, its application in civil engineering is becoming very wide and promising. Varied inerter mechanisms have already been tested and applied to further enhance the control performance of conventional energy dissipation, vibration absorption, and seismic isolation designs and to overcome the inevitable difficulties encountered in them [18, 19]. Of these, inerter-based seismic isolation designs, devices, and systems with series, parallel, and hybrid configurations for passive control, which are relevant to the scope of this study, are reviewed. Several inerter-based seismic isolation configurations have been analytically and numerically investigated [20, 21], in which the mechanical behavior of the seismic isolation system is represented by a linear spring element and a dashpot element connected in parallel. These studies have demonstrated that using an inerter with the same inertance-to-mass ratio in any of the configurations has superior control performance compared with traditional seismic isolation designs. Based on the proposed H_{∞} and H_2 optimization procedures [20], it has been suggested that the simplest configuration (i.e., that the inerter and the seismic isolation system are directly mounted in parallel) already has sufficiently wide suppression bandwidth owing to its negative stiffness and antiresonance effects. Other sophisticated layouts have been proposed and verified to be more effective at reducing the seismic responses of seismic isolation systems and superstructures. Note that the acceleration control performance of inerter-based seismic isolation designs at a higher frequency range may be compromised; i.e., there is effective suppression of isolation displacement but augmented acceleration transmitted to the seismically isolated superstructure because of a more significant generated inerter force [20, 21]. This means that the excessive force generated by an inerter should receive special attention when designing a seismic isolation device and system.

Many studies [22–26] have considered a variety of earthquake scenarios to demonstrate the efficacy of incorporating a conventional tuned mass damper (TMD) into a seismic isolation design for reducing the seismic demand of the isolation system and the seismic response of the isolated superstructure, with an emphasis on the former. It appears that a sufficiently weighty tuned mass is required to enable the storage of enough input energy to achieve satisfactory control performance, but this may introduce issues with space use and cost. This can be easily understood from the case study of De Domenico and Ricciardi [26]. On the premise of avoiding adding considerable mass, the design of an inerter as a secondary oscillator to store input energy and protect the primary target from unacceptable vibration is one of the most effective strategies required to overcome the aforementioned difficulties. Some studies [27–33] proposed mounting an inerter-based TMD system in which there is still a physical tuned mass block (i.e., the so-called tuned mass damper inerter or TMDI), and others [34–42] proposed mounting an inerter system in which there is no physical tuned mass block (i.e., the so-called tuned inerter damper or TID, which is the simplest design) between the ground and the target to be protected. Different equations of motion and optimization design procedures for various TMDI and TID designs and configurations have been developed and numerically and experimentally demonstrated with a fair basis of comparison. In addition to verifying that adopting an inerter with the same inertance-to-mass ratio in any mechanism and configuration achieves superior control performance to the traditional TMD design (reduction of isolation displacement in particular), comparisons with other vibration absorption designs, such as tuned liquid column dampers (TLCDs) [33], have also been made to further emphasize the distinct advantages of inerters.

In the aforementioned studies [27–42], one terminal of the proposed TMDI or TID system was connected with the ground, and the other terminal was designed to be mounted above [27, 30, 33] or below the base floor of the seismically isolated structure [28, 31, 33, 37–40] or laterally attached to it [29, 32, 34–36, 41, 42]. Besides linearly elastic seismic isolation systems, nonlinear plastic systems that use different hysteretic models (e.g., Coulomb friction and Bouc-Wen hysteretic models [28]), and seismic isolation systems composed of specific bearings (e.g., lead rubber bearings (LRBs) [39] and friction pendulum bearings (FPBs)) [34, 37] have also been incorporated into the analytical, numerical, and experimental models. When incorporating TMDIs into seismic isolation systems, it has been further shown that TMDIs are very suitable for nonlinear systems without any adverse effect arising from detuning [28], which overcomes the drawbacks of the traditional TMD design (i.e., the high sensitivity of control performance to the tuning frequency and earthquake frequency content). It has also been recommended that the design of a larger inertance and lower added tuned mass be implemented to improve control performance as well as a seismic isolation system with lower damping [29].

From the reviewed literature, it is clear that the use of an inerter for passive seismic isolation has attracted immense

attention in the earthquake engineering field. However, the combination of SRBs, which mechanically present twin-flag hysteretic behavior, with an inerter has not yet been studied. Differing from previous theoretical studies [4–6], the inertial and restoring forces generated by the rotational motion of the cylindrical roller of a typical existing SRB (i.e., the inherent rotational mass) is the first considered to derive more exact equations of motion for SRBs with nonnegligible roller mass, which are denoted as IRM-SRBs hereafter. The dynamic responses of several IRM-SRB models with different design parameters under harmonic excitations of various acceleration amplitudes and periods are numerically discussed. Then, the design mechanism of an SRB combined with an externally added rotational inerter, denoted as ARI-SRB hereafter, is introduced and the corresponding equations of motion are deduced. A series of numerical studies using harmonic excitation and ground motion are conducted to further understand the dynamic characteristics, behavior, and control performance of ARI-SRBs. A simple, practical, and acceleration-based design procedure for ARI-SRBs is then proposed based on the parametric and numerical analysis results. A simple but practical example is provided for further examining the feasibility of the proposed design procedure.

Section 2 of this paper briefly introduces SRBs and IRM-SRBs. Based on the derived equations of motion for IRM-SRBs, a parametric study under harmonic excitation is described to better understand the mechanical behavior of

IRM-SRBs and the adverse effects of neglecting the roller mass of SRBs. Section 3 introduces the design of ARI-SRBs. Based on the derived equations of motion for ARI-SRBs, a parametric study using harmonic excitation and a numeric study using ground motion to better understand the mechanical behavior as well as the control performance of ARI-SRBs are described. Section 4 proposes an acceleration-based procedure for designing ARI-SRBs in an easy and practical manner and also provides a design example. Some conclusions are provided in Section 5.

2. SRBs That Consider Inherent Rotational Mass (IRM-SRBs)

2.1. Generalized Analytical Models of SRBs That Do Not Consider Inherent Rotational Mass. For SRBs designed with single sloping angles and friction damping forces, Figure 1(a) presents a simplified model for SRBs consisting of an upper bearing plate, a roller, and a lower bearing plate in one principle horizontal direction, and Figure 2 presents the free body diagram of the simplified model shown in Figure 1(a) when $\mathrm{sgn}(x_u) = \mathrm{sgn}(x_r) = 1$ and $\mathrm{sgn}(\dot{x}_u) = \mathrm{sgn}(\dot{x}_r) = 1$. Based on the free body diagram, four dynamic force equilibrium equations, one dynamic moment equilibrium equation, and four compatibility conditions can be obtained as given in equations (1) to (9) [4–6] to solve a total of nine variables of α, $\ddot{x}_u$, $\ddot{x}_r$, $\ddot{z}_u$, $\ddot{z}_r$, N_u, N_l, f_u, and f_l.

$$-(F_D \cos \theta_u + f_u \cos \theta_u)\mathrm{sgn}(\dot{x}_u) - N_u \sin \theta_u \mathrm{sgn}(x_u) = m(\ddot{x}_u + \ddot{x}_g), \tag{1}$$

$$-(F_D \sin \theta_u + f_u \sin \theta_u)\mathrm{sgn}(x_u)\mathrm{sgn}(\dot{x}_u) + N_u \cos \theta_u - mg = m(\ddot{z}_u + \ddot{z}_g), \tag{2}$$

$$(F_D \cos \theta_u - F_D \cos \theta_l + f_u \cos \theta_u - f_l \cos \theta_l)\mathrm{sgn}(\dot{x}_u) + (N_u \sin \theta_u - N_l \sin \theta_l)\mathrm{sgn}(x_u) = m_r(\ddot{x}_r + \ddot{x}_g), \tag{3}$$

$$(F_D \sin \theta_u - F_D \sin \theta_l + f_1 \sin \theta_1 - f_2 \sin \theta_2)\mathrm{sgn}(x_u)\mathrm{sgn}(\dot{x}_u) - N_1 \cos \theta_1 + N_2 \cos \theta_2 - m_r g = m_r(\ddot{z}_r + \ddot{z}_g), \tag{4}$$

$$r(f_u + f_l)\mathrm{sgn}(\dot{x}_u) = I\alpha, \tag{5}$$

$$\ddot{x}_r = r\alpha \cos \theta_l, \tag{6}$$

$$\ddot{z}_r = r\alpha \sin \theta_l \mathrm{sgn}(x_u), \tag{7}$$

$$\ddot{x}_u = \ddot{x}_l + r\alpha \cos \theta_u = r\alpha(\cos \theta_u + \cos \theta_l), \tag{8}$$

$$\ddot{z}_u = \ddot{z}_r + r\alpha \sin \theta_u \mathrm{sgn}(x_u) = r\alpha(\sin \theta_u + \sin \theta_l)\mathrm{sgn}(x_u), \tag{9}$$

where x_u, $\dot{x}_u$, and $\ddot{x}_u$ are the horizontal displacement, velocity, and acceleration responses of the protected object and upper bearing plate relative to ground (or the fixed lower bearing plate); z_u, $\dot{z}_u$, and $\ddot{z}_u$ are the vertical displacement, velocity, and acceleration responses of the protected object and upper bearing plate relative to ground (or the fixed lower bearing plate); x_r (z_r), $\dot{x}_r$ ($\dot{z}_r$), and $\ddot{x}_r$ ($\ddot{z}_r$) are the

horizontal (and vertical) displacement, velocity, and acceleration responses of the roller relative to ground (or the fixed lower bearing plate); $\ddot{x}_g$ ($\ddot{z}_g$) is the horizontal (and vertical) acceleration of the excitation; g is the acceleration due to gravity; m and m_r are the total mass of the protected object and upper bearing plate and the mass of the roller, respectively; r is the radius of the roller; θ_u and θ_l are the

sloping angles designed for the rolling surfaces of the upper and lower bearing plates, respectively; I is the moment of inertia of the roller $= 1/2\, m_r r^2$; α is the angular acceleration of the roller (where clockwise rotation is positive); f_u (f_l) and N_u (N_l) are the rolling friction force and normal force acting between the upper bearing plate and roller (and between the roller and lower bearing plate), respectively; and F_D is the built-in friction damping force acting parallel to the slope of the bearing plates, which is usually simulated by a Coulomb friction model for simplicity.

Based on the assumptions of very small designed sloping angles, the roller being much lighter than the object to be protected above it (i.e., $m_r/m \approx 0$), and with no applied vertical disturbance (i.e., $\ddot{z}_g = 0$), the horizontal transmitted constant acceleration when the cylindrical roller is in motion within the sloped rolling range can be further obtained in a simplified and linearized form as given in equation (10) [4–6]. In other words, the following equation is the equation of motion of SRBs when the roller is out of the arc rolling range d.

$$\ddot{x}_u + \ddot{x}_g = -\frac{1}{2}g(\theta_u + \theta_l)\mathrm{sgn}(x_u) - \frac{F_D}{m}\mathrm{sgn}(\dot{x}_u). \tag{10}$$

To avoid pounding when the roller passes through the intersection of the two inclines of the V-shaped surfaces of the bearing plates, an arc rolling range with a fixed curvature radius (R) is provided [4]. If the surfaces of the two bearing plates in contact with the roller are designed to be sloped, i.e., both θ_u and θ_l are not equal to zero (Figure 1(b)), the horizontal transmitted acceleration of an SRB when the

roller is in motion within the arc rolling range d in a simplified and linearized form is obtained from [4–6]:

$$\ddot{x}_u + \ddot{x}_g = -\frac{g}{2R}x_u - \frac{F_D}{m}\mathrm{sgn}(\dot{x}_u). \tag{11}$$

If one of the surfaces of the two bearing plates in contact with the roller is designed to be flat, i.e., either θ_u or θ_l is equal to zero (Figure 1(c)), the horizontal transmitted acceleration of an SRB when the roller is in motion within the arc rolling range d in a simplified and linearized form is obtained from [4–6]:

$$\ddot{x}_u + \ddot{x}_g = -\frac{g}{4R}x_u - \frac{F_D}{m}\mathrm{sgn}(\dot{x}_u). \tag{12}$$

The typical twin-flag hysteretic behavior of SRBs designed with single sloping angles and friction damping forces, which can be quantitatively obtained using equations (10) to (12), is schematically presented in Figure 3 [4–7].

2.2. Generalized Analytical Models of IRM-SRBs. As described in Section 2.1, equations (10) to (12) are obtained by ignoring the inertial and restoring forces generated by the rotational motion of the existing roller. With the same simplifying assumptions made in Section 2.1, except for retaining the roller mass during derivation (i.e., $m_r/m \neq 0$) and by further defining the mass ratio $R_m = m_r/m$, the horizontal acceleration of IRM-SRBs relative to ground when the roller is in motion within the sloped rolling range can be obtained from:

$$
\begin{aligned}
\ddot{x}_u &= \frac{-1}{(m + 3/8 m_r)}\left[F_D\mathrm{sgn}(\dot{x}_u) + \left(m + \frac{1}{2}m_r\right)\ddot{x}_g + \frac{1}{2}mg(\theta_u + \theta_l)\mathrm{sgn}(x_u) + \frac{1}{2}m_r g\theta_l\mathrm{sgn}(x_u)\right], \\
&= \frac{-1}{(1 + 3/8 R_m)m}\left[F_D\mathrm{sgn}(\dot{x}_u) + \left(1 + \frac{1}{2}R_m\right)m\ddot{x}_g + \frac{1}{2}mg(\theta_u + \theta_l)\mathrm{sgn}(x_u) + \frac{1}{2}R_m mg\theta_l\mathrm{sgn}(x_u)\right].
\end{aligned}
\tag{13}
$$

When both θ_u and θ_l are not equal to zero (Figure 1(b)), the horizontal acceleration of IRM-SRBs relative to the ground when the roller is in motion within the arc rolling range d is obtained from the following equations:

$$
\begin{aligned}
\ddot{x}_u &= \frac{-1}{(m + 3/8 m_r)}\left[F_D\mathrm{sgn}(\dot{x}_u) + \left(m + \frac{1}{2}m_r\right)\ddot{x}_g + \left(m + \frac{1}{2}m_r\right)\frac{gx_u}{2R}\right], \\
&= \frac{-1}{(1 + 3/8 R_m)m}\left[F_D\mathrm{sgn}(\dot{x}_u) + \left(1 + \frac{1}{2}R_m\right)m\ddot{x}_g + \left(1 + \frac{1}{2}R_m\right)\frac{mgx_u}{2R}\right].
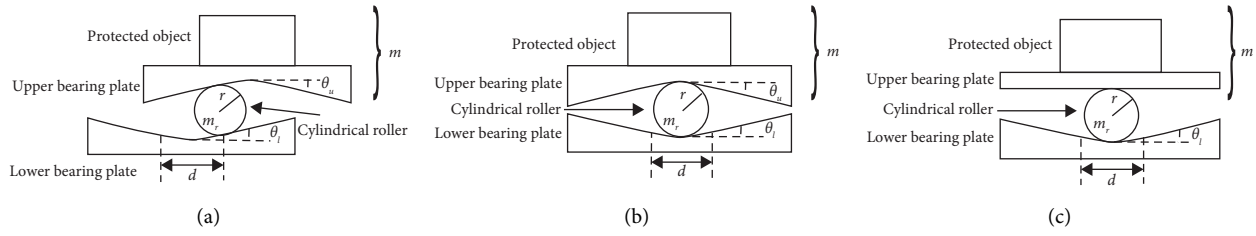\end{aligned}
\tag{14}
$$

FIGURE 1: A simplified model for SRBs with one principle horizontal direction. (a) In the sloped rolling range. (b) In the arc rolling range (θ_u, $\theta_l \neq 0$). (c) In the arc rolling range (either θ_u or $\theta_l = 0$).
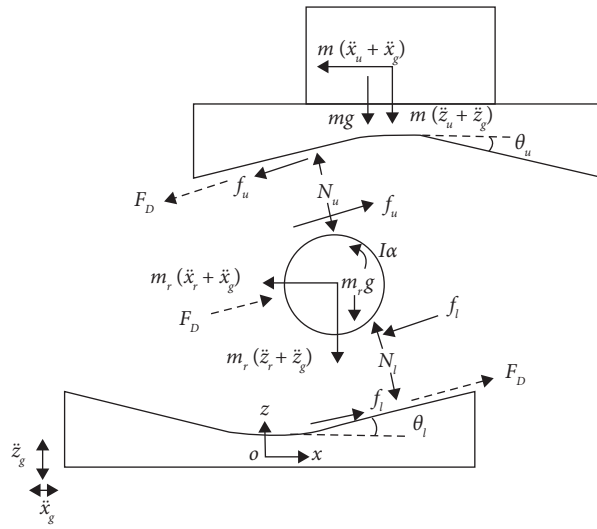

FIGURE 2: Free body diagram of the simplified model when $\text{sgn}(x_u) = \text{sgn}(x_r) = 1$ and $\text{sgn}(\dot{x}_u) = \text{sgn}(\dot{x}_r) = 1$.
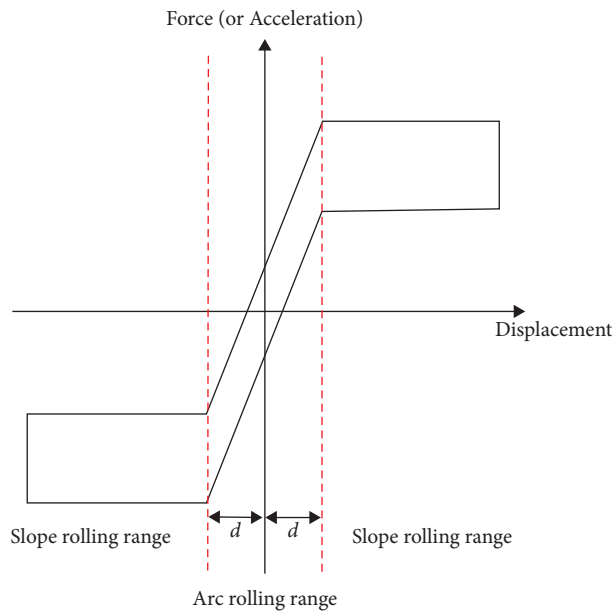

FIGURE 3: Typical hysteretic behavior of SRBs designed with single sloping angles and friction damping forces [4–7].

When either θ_u or θ_l is equal to zero (Figure 1(c)), the horizontal acceleration of IRM-SRBs relative to the ground when the roller is in motion within the arc rolling range d is obtained from the following equations:

$$
\begin{aligned}
\ddot{x}_u &= \frac{-1}{(m + 3/8m_r)}\left[F_D\mathrm{sgn}(\dot{x}_u) + \left(m + \frac{1}{2}m_r\right)\ddot{x}_g + (m + m_r)\frac{gx_u}{4R}\right], \\
&= \frac{-1}{(1 + 3/8R_m)m}\left[F_D\mathrm{sgn}(\dot{x}_u) + \left(1 + \frac{1}{2}R_m\right)m\ddot{x}_g + (1 + R_m)\frac{mgx_u}{4R}\right].
\end{aligned}
\tag{15}
$$

By comparing equations (13) to (15) with equations (10) to (12), consideration of the inherent rotational mass not only equivalently contributes to the inertial force represented in the denominator on the right-hand side of the equalities but also affects the restoring force represented inside the bracket on their right-hand side. In other words, in addition to changing the inertial force, consideration of the inherent rotational mass also changes the restoring force. Based on the equations of motion given in equations (10) to (12) and equations (13) to (15), and considering the relative static state when the designed friction force is larger than the critical friction (obtained by setting $\ddot{x}_u = 0$ during numerical integration), the acceleration and displacement responses of SRBs and IRM-SRBs under external disturbance can be numerically analyzed.

2.3. Parametric Study of IRM-SRBs under Harmonic Excitation

2.3.1. Harmonic Excitation.
To study the steady-state responses of IRM-SRBs under an external disturbance, unilateral periodic harmonic excitation with an amplitude that linearly increases until reaching a target acceleration amplitude is considered herein and expressed as follows:

$$
\ddot{x}_g = A_0\sin\left(\frac{2\pi}{T_g}\right)t, \quad A_0 = \begin{cases} \dfrac{A_g}{T_0}t, & \text{when } t \leq T_0, \\[2ex] A_g, & \text{when } T_0 < t < T, \end{cases}
\tag{16}
$$

where A_0 is the acceleration amplitude of the unilateral periodic harmonic excitation; T_g is the harmonic excitation period; A_g is the target acceleration amplitude; T_0 is the time needed for the acceleration amplitude to reach the target; and T is the total duration of the external disturbance. The value of T_0 is taken as 25 times the period of the harmonic excitation (i.e., $T_0 = 25T_g$) in order to minimize the effect of the transient responses. The value of T is taken as 200 times the period of the harmonic excitation (i.e., $T = 200T_g$) for the same purpose. The amplitude of the harmonic excitation versus time is presented in Figure 4.

2.3.2. First Parametric Study Results and Discussion.
Another normalized factor obtained by dividing F_D by mg is further defined and denoted as μ^*. The first parametric study for IRM-SRBs aimed to probe the variation of their peak acceleration and displacement responses with respect to R_m. Let $m = 1$ ton, $\theta_u = 0$ degrees, $\theta_l = 3$ degrees, $\mu^* = 0.0561$ (i.e., $F_D = 550$ N), $R = 0.1$ m, and $d = 0.0105$ m, which are frequently used values for the practical design of SRBs. Eleven sets of R_m in total, including one SRB model with $R_m = 0$ (i.e., $m_r = 0$ kg) and ten IRM-SRB models with $R_m = 0.0, 0.05, 0.1, 0.15, 0.2, 0.25, 0.3, 0.35, 0.4, 0.45,$ and 0.5 (i.e., $m_r = 0, 50, 100, 150, 200, 250, 300, 350, 400, 450,$ and 500 kg, respectively), were considered. Unilateral periodic harmonic excitations with $A_g = 0.3$ g and $T_g = 1$ s were used. Note that the horizontal transmitted constant acceleration designed for the SRB model was calculated from equation (10) as 0.0822 g. In addition, very large values of R_m (i.e., very large cylindrical rollers) may not be practically feasible for current SRB design mechanisms. The assumed parameters and excitation for the first parametric study of IRM-SRBs are listed in Table 1.

The 3-cycle hysteretic loops under harmonic excitation of the SRB model with $R_m = 0$ (obtained using equations (10) to (12)) and those of the IRM-SRB models with different values of R_m (obtained using equations (13) to (15)) are correspondingly represented by black and blue lines in Figure 5(a), for which the darker blue color represents a larger value of R_m, and the abscissa and ordinate represent the relative displacement and absolute acceleration responses, respectively. To better understand the occurrence sequence of certain crucial relative displacement, relative velocity, and absolute acceleration responses, the corresponding absolute acceleration responses versus the relative velocity responses are presented in Figure 5(b), and the same symbol represents the same approximate time point during the numerical integration in Figures 5(a) and 5(b). To better and quantitatively compare the contributions of increasing roller mass to the restoring force and inertial force of the IRM-SRB models, two hysteresis loops plotted with green dotted lines, which represent the results of setting $R_m = 0.05$ (lighter green color) and 0.5 (darker green color) but ignoring the term R_m inside the bracket on the right-hand side
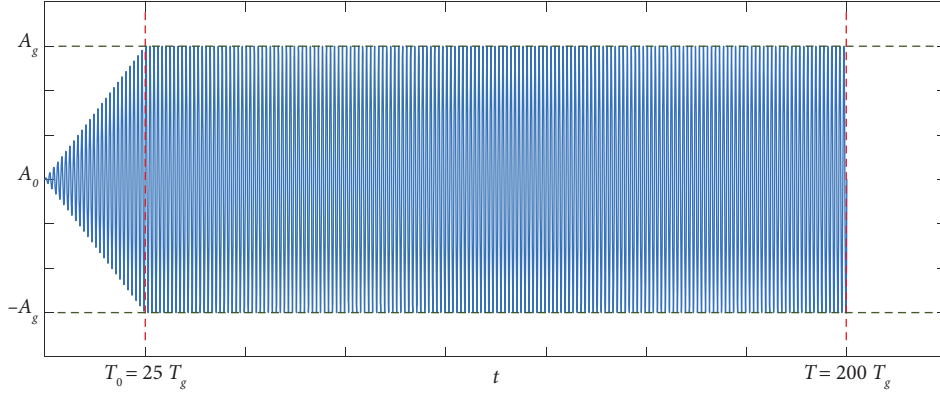
FIGURE 4: Harmonic excitation history.

of equations (13) to (15) during numerical integration, are also provided in Figures 5(a) and 5(b). Evidently, the difference between the results with and without considering R_m (inside the bracket on the right-hand side of equations (13) to (15)) is very noticeable. It is thus numerically demonstrated that increasing roller mass contributes more significantly to the restoring force than to the inertial force thus lessening the advantage of increasing the inherent rotational mass if indeed there is any.

Variations of the peak acceleration and displacement responses of the IRM-SRB models with respect to R_m are shown in Figures 5(c) and 5(d), respectively. It is evident that the larger the value of R_m, the more significant is the effect. A heavier roller or a larger inherent rotational mass (i.e., a larger value of m_r or R_m) mechanically generates a more significant restoring force and leads to larger acceleration and displacement responses when the roller is in motion within the sloped rolling range. The peak acceleration responses appear to exceed the horizontal transmitted constant acceleration designed for the SRB model (0.0822 g). The numbers shown in Figures 5(c) and 5(d), which are correspondingly calculated as per equations (17) and (18), indicate the errors in peak acceleration and displacement responses caused by neglecting the influence of the roller mass of SRBs, respectively. It is evident that the larger the value of R_m, the greater the underestimation extent of peak acceleration and displacement responses. For the worst case here, the peak acceleration and displacement responses are underestimated by 16.712% (with $R_m = 0.5$) and 7.021% (with $R_m = 0.5$), respectively.

$$\text{Err}_a = \left(\frac{A_{\text{IRM-SRB}}}{A_{\text{SRB}}} - 1 \right) \times 100\%, \tag{17}$$

$$\text{Err}_d = \left(\frac{D_{\text{IRM-SRB}}}{D_{\text{SRB}}} - 1 \right) \times 100\%, \tag{18}$$

where Err_a and Err_d are the indices to quantitatively estimate the errors in peak acceleration and displacement responses caused by neglecting the influence of the roller mass of SRBs, respectively; $A_{\text{IRM-SRB}}$ and $D_{\text{IRM-SRB}}$ are the peak acceleration and displacement responses of an IRM-SRB, respectively; and A_{SRB} and D_{SRB} are the peak acceleration and displacement responses of an SRB, respectively.

2.3.3. Second Parametric Study Results and Discussion. The second parametric study of IRM-SRBs aimed to probe the dependencies of their peak acceleration and displacement responses on A_g. Let $m = 1$ ton, $\theta_u = 0$ degrees, $\theta_l = 3$ degrees, $\mu^* = 0.0561$ (i.e., $F_D = 550$ N), $R = 0.1$ m, $d = 0.0105$ m, and $R_m = 0$ (i.e., an SRB model) and 0.2 (i.e., an IRM-SRB model). Unilateral periodic harmonic excitations with $T_g = 1$ s but values of A_g varying from 0.1 g to 1 g with an increment of 0.1 g were used. Details of the assumed parameters and the excitations used for the second parametric study of IRM-SRBs are listed in Table 1. The 3-cycle hysteretic loops under harmonic excitation of the SRB model (with $R_m = 0$) and the IRM-SRB model (with $R_m = 0.2$) correspondingly obtained using equations (10) to (12) and equations (13) to (15) are presented in Figure 6(a). Variations of the peak acceleration and displacement responses of the SRB and IRM-SRB models with respect to A_g are shown in Figures 6(b) and 6(c), respectively.

As explained in Section 2.3.2, because the IRM-SRB model mechanically generates a restoring force when the roller is in motion within the sloped rolling range, whereas the SRB model does not, it has larger acceleration and displacement responses under the same harmonic excitation. The peak acceleration responses of the IRM-SRB model exceed the horizontal transmitted constant acceleration designed for the SRB model (0.0822 g). The peak acceleration and displacement responses of the IRM-SRB model are approximately linearly proportional to A_g, and so are the peak displacement responses of the SRB model [6]. The numbers shown in Figures 6(b) and 6(c), which are correspondingly calculated as per equations (17) and (18), indicate the errors in peak acceleration and displacement responses caused by neglecting the influence of the roller mass of SRBs, respectively. It is evident that the larger the value of A_g, the severer is the underestimation extent of peak acceleration responses. Except for $A_g = 0.1$ g, the effect of A_g

Table 1: Assumed parameters and excitations for the parametric studies (including the inherent rotational mass and the added rotational inerter).

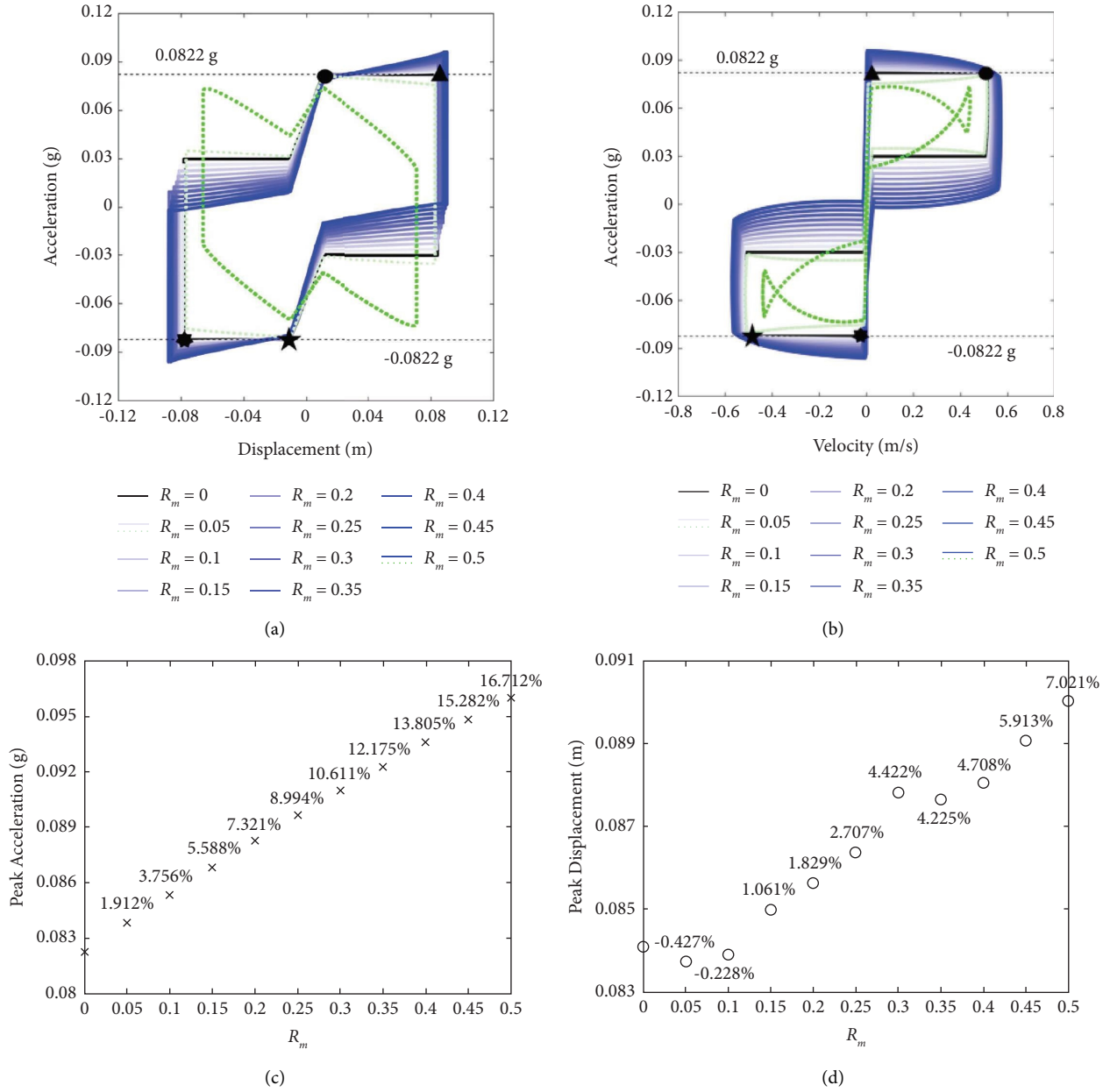| Parameters		First	Second	Third
m (ton)			1	
θ_u (degrees)			0	
θ_l (degrees)			3	
μ^*			0.0561	
R (m)			0.1	
d (m)			0.0105	
R_m	IRM-SRB	0, 0.05, 0.1, 0.15, 0.2, 0.25, 0.3, 0.35, 0.4, 0.45, 0.5		0, 0.2
	ARI-SRB		0.005	
β (ARI-SRB)		0, 0.05, 0.1, 0.15, 0.2, 0.25, 0.3, 0.35, 0.4, 0.45		0.45, 0.24 0.16, 0.1
A_g (g)	IRM-SRB	0.3		0.3
	ARI-SRB	0.2, 0.3, 0.4, 0.6	0.1, 0.2, 0.3, 0.4, 0.5, 0.6, 0.7, 0.8, 0.9, 1	0.2, 0.3, 0.4, 0.6
T_g (s)	IRM-SRB	1	1	0.1, 0.2, 0.3, 0.4, 0.5, 0.6, 0.7, 0.8, 0.9, 1, 2, 3, 4, 5, 6, 7, 8, 9, 10
	ARI-SRB			

(a)

(b)

(c)

(d)

FIGURE 5: Effect of inherent rotational mass with different R_m on the control performance of IRM-SRB models under harmonic excitation with $A_g = 0.3$ g and $T_g = 1$ s. (a) Absolute acceleration versus relative displacement. (b) Absolute acceleration versus relative velocity. (c) Peak acceleration versus R_m. (d) Peak displacement versus R_m.

on the underestimation extent of peak displacement responses is less insignificant. For the worst case here, the peak acceleration and displacement responses are underestimated by 27.713% (with $A_g = 1$ g) and 14.094% (with $A_g = 0.1$ g), respectively.

2.3.4. Third Parametric Study Results and Discussion. The third parametric study for IRM-SRBs aimed to probe the dependencies of their peak acceleration and displacement responses on T_g. The values set for m, θ_u, θ_b, μ^*, R, d, and R_m are identical to those in Section 2.3.3. Unilateral periodic harmonic excitations with $A_g = 0.3$ g but values of T_g

varying from 0.1 s to 1 s with an increment of 0.1 s and varying from 1 s to 10 s with an increment of 1 s were used. Details of the parameters assumed and the excitations considered for the third parametric study of IRM-SRB are listed in Table 1. The 3-cycle hysteresis loops under harmonic excitation of the SRB model (with $R_m = 0$) and the IRM-SRB model (with $R_m = 0.2$) are presented in Figures 7(a) and 7(b). Variations of the peak acceleration and displacement responses of the SRB and IRM-SRB models with respect to T_g are shown in Figures 7(c) and 7(d), respectively.

The T_g dependency observed here is basically identical to the A_g dependency observed in Section 2.3.3. Because the
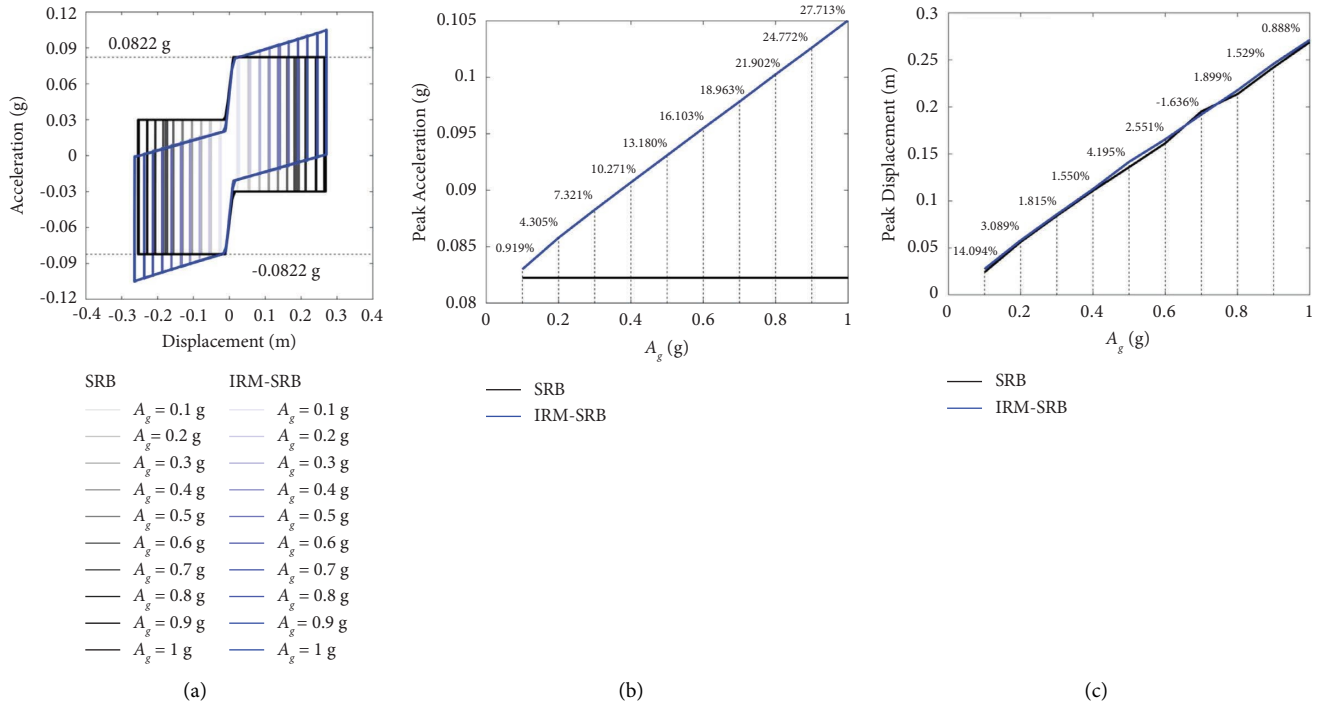
FIGURE 6: Effect of varying A_g on the control performance of SRBs and IRM-SRBs. (a) Hysteresis loops. (b) Peak acceleration versus A_g. (c) Peak displacement versus A_g.
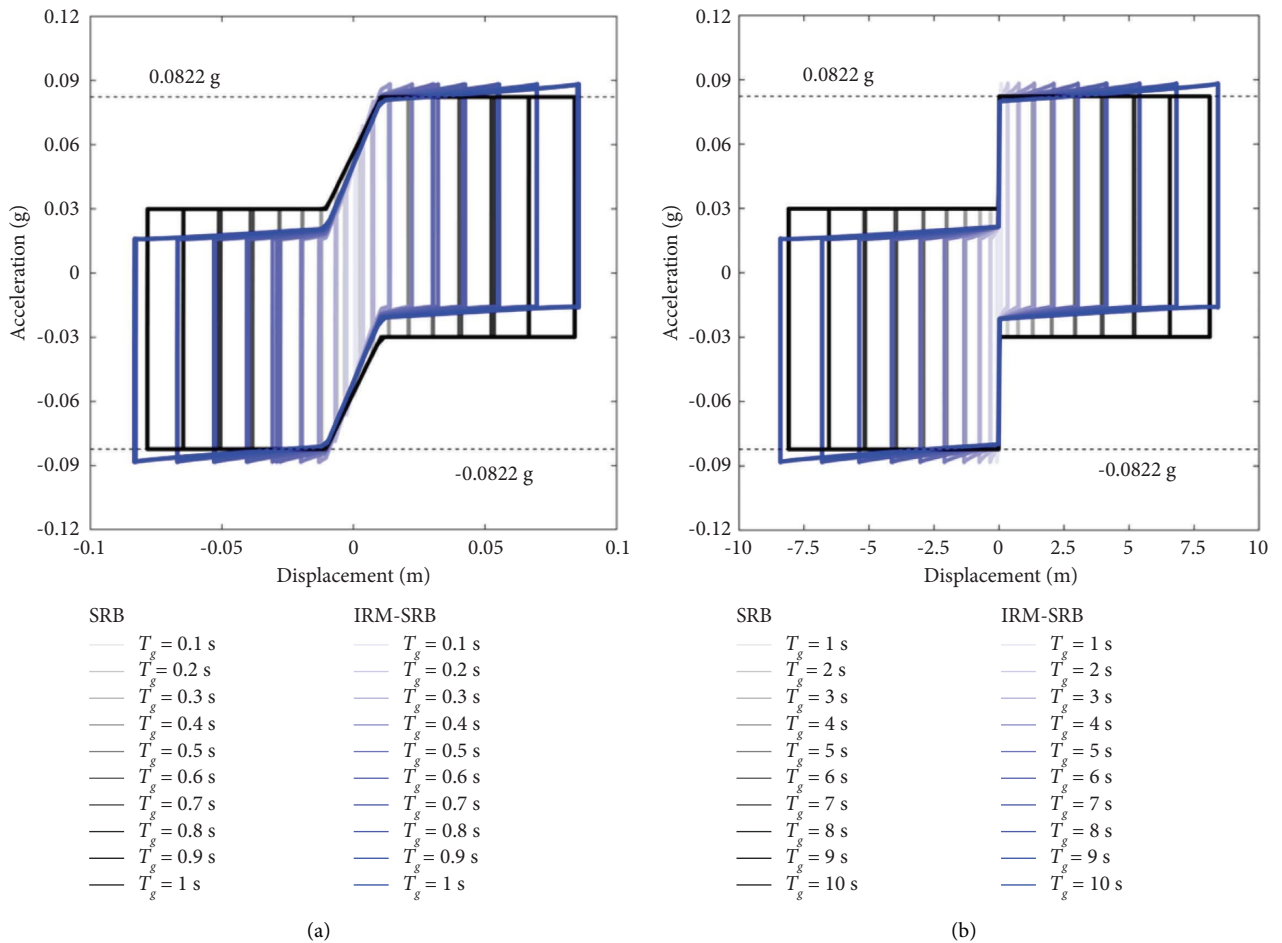
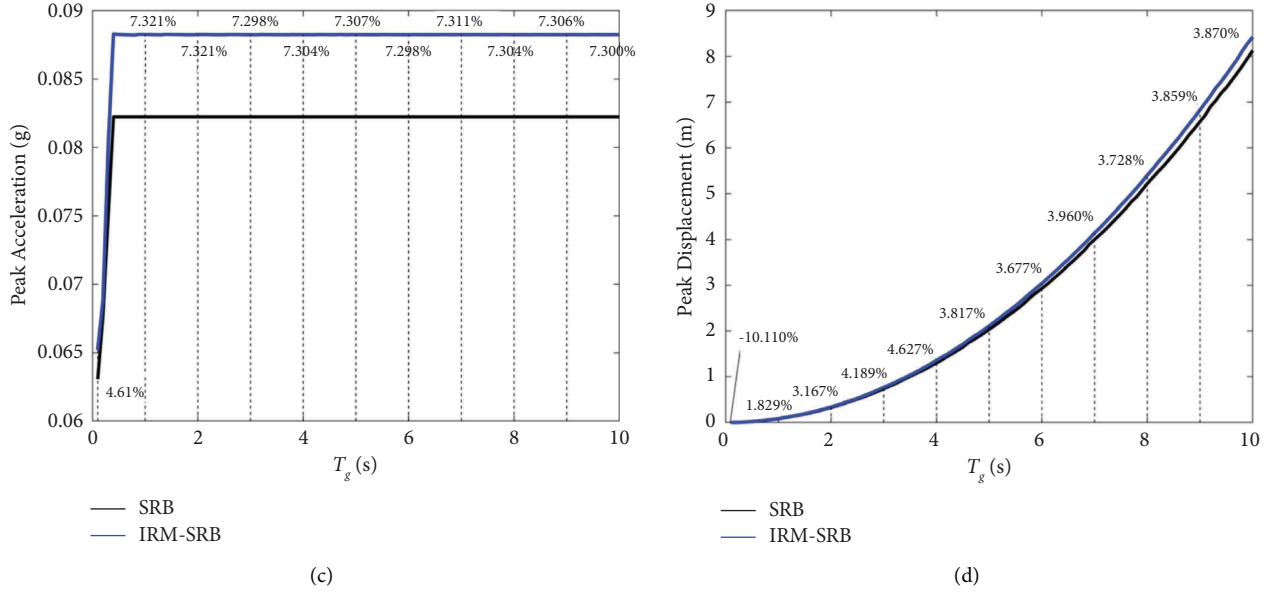

FIGURE 7: Continued.

(c)

(d)

FIGURE 7: Effect of varying T_g on the control performance of SRBs and IRM-SRBs. (a) Hysteresis loops ($T_g = 0.1$ s to 1 s). (b) Hysteresis loops ($T_g = 1$ s to 10 s). (c) Absolute acceleration versus T_g. (d) Relative displacement versus T_g.

IRM-SRB model mechanically generates a restoring force when the roller is in motion within the sloped rolling range whereas the SRB model does not, it has larger acceleration and displacement responses under the same harmonic excitation. The peak acceleration responses of the IRM-SRB model exceed the horizontal transmitted constant acceleration designed for the SRB model (0.0822 g) when the value of T_g is not too small. Here, when $T_g \leq 0.3$ s, the roller is still in motion within the arc rolling range and so shows peak acceleration responses smaller than 0.0822 g for the IRM-SRB model. Note that the difference compared with the A_g dependency is that the peak displacement responses of the SRB and IRM-SRB model increase with T_g but not linearly, and the peak acceleration responses of both models are independent of T_g when the value of T_g is not too small (i.e., $T_g \geq 0.4$ s) or when the roller is in motion within the sloped rolling range. The numbers shown in Figures 7(c) and 7(d), which are correspondingly calculated as per equations (17) and (18), indicate the errors in peak acceleration and displacement responses caused by neglecting the influence of the roller mass of SRBs, respectively. It is evident that when the roller is in motion within the sloped rolling range, the underestimation extent of peak acceleration and displacement responses is not greatly dependent on T_g. For the worst case here, the peak acceleration and displacement responses are underestimated by 7.321% (with $T_g = 1$ and 2 s) and 4.627% (with $T_g = 4$ s), respectively.

The observed phenomena for IRM-SRBs under harmonic excitation are very constructive and motivate further study on the seismic performance of SRBs with added rotational inerters (introduced and discussed in Section 3), which is a more feasible practical method for amplifying the inertial force, and corresponding superior control performance.

3. SRBs with an Added Rotational Inerter (ARI-SRBs)

It was numerically demonstrated in Section 2 that the effect of the inertial force generated by the rotational motion of the roller of existing SRBs on the overall performance is not very significant when considering practically feasible dimensions. Other than simply increasing the roller mass without limit, which is practically impossible, the mass increase contributes less significantly to the inertance than to the restoring force. Therefore, by referring to the design mechanism proposed by Smith [14] to enlarge the angular velocity and reduce the mass of the inerter as much as possible (Figure 8), it is attempted in this section to connect SRBs directly with a rotational inerter in parallel (ARI-SRBs). In Figure 8, the added rotational inerter (i.e., the flywheel) is mechanically driven by a rack, one gear wheel (or more if practically feasible), and two pinions (or more if practically feasible). As indicated in Figure 8, r_{gw}, r_{rp}, r_{fp}, and r_f are the radii of the gear wheel, rack-pinion, flywheel pinion, and flywheel, respectively, and m_I is the mass of the flywheel (i.e., the added rotational inerter).

3.1. Analytical Models of an ARI-SRB. The inertial and restoring forces generated by the rotational motion of the existing roller with a suitable mass as described in Section 2.2 are still appropriately considered in this analysis. The conceptual design mechanism of the added rotational inerter is similar to that proposed by Smith [14], and its two terminals are assumed to be correspondingly connected to the upper and lower bearing plates of the SRB in each principle horizontal direction (see Figure 9, in which two sets of inerters are connected with the SRB in parallel). The horizontal acceleration of ARI-SRBs relative to the ground when
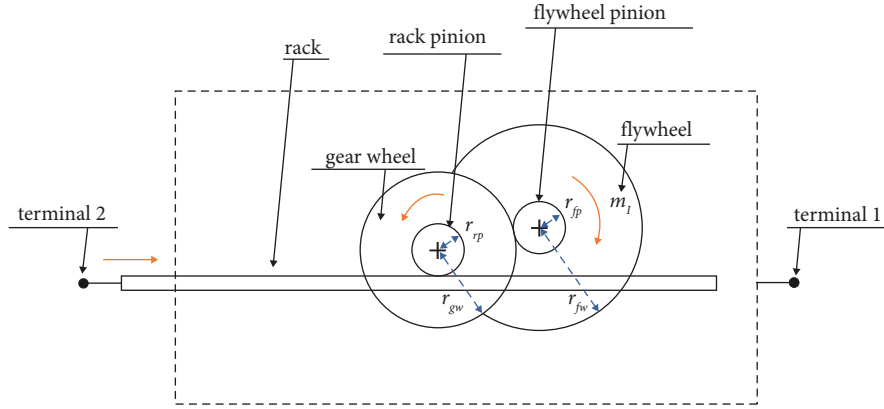
FIGURE 8: Conceptual design of the mechanism of an added rotational inerter [14].

the roller is in motion within the sloped rolling range can be obtained as in equation (20) by further defining the inertance b contributed by the added rotational inerter and a ratio of the inertance to the total mass of the protected object plus the upper bearing plate of the SRB (i.e., the inertance factor $\beta = b/m$) as in equation (19), obtained in a simplified form by assuming the masses of the rack, gear wheel, and pinions shown in Figure 8 are negligible. The

inertial force induced by the added rotational inerter in equation (19) is also incorporated into the derivation.

$$b\ddot{x}_u = \beta m\ddot{x}_u = \frac{1}{2}m_I\left(\frac{r_{\mathrm{gw}}r_{\mathrm{fw}}}{r_{\mathrm{rp}}r_{\mathrm{fp}}}\right)^2\ddot{x}_u = \frac{1}{2}m_I\gamma_m^2\ddot{x}_u, \quad (19)$$

where $\gamma_m = (r_{\mathrm{gw}}r_{\mathrm{fw}}/r_{\mathrm{rp}}r_{\mathrm{fp}})$.

$$\ddot{x}_u = \frac{-1}{(1 + 3/8R_m)m + b}\left[F_D\mathrm{sgn}(\dot{x}_u) + \left(1 + \frac{1}{2}R_m\right)m\ddot{x}_g + \frac{1}{2}\mathrm{mg}(\theta_u + \theta_l)\mathrm{sgn}(x_u) + \frac{1}{2}R_m\mathrm{mg}\theta_l\mathrm{sgn}(x_u)\right],$$

$$= \frac{-1}{(1 + 3/8R_m + \beta)m}\left[F_D\mathrm{sgn}(\dot{x}_u) + \left(1 + \frac{1}{2}R_m\right)m\ddot{x}_g + \frac{1}{2}\mathrm{mg}(\theta_u + \theta_l)\mathrm{sgn}(x_u) + \frac{1}{2}R_m\mathrm{mg}\theta_l\mathrm{sgn}(x_u)\right]. \quad (20)$$

When both θ_u and θ_l are not equal to zero (Figure 1(b)), the horizontal acceleration of an ARI-SRB relative to ground when the roller is in motion within the arc rolling range d is obtained from the following equation:

$$\ddot{x}_u = \frac{-1}{(1 + 3/8R_m)m + b}\left[F_D\mathrm{sgn}(\dot{x}_u) + \left(1 + \frac{1}{2}R_m\right)m\ddot{x}_g + \left(1 + \frac{1}{2}R_m\right)\frac{\mathrm{mg}x_u}{2R}\right],$$

$$= \frac{-1}{(1 + 3/8R_m + \beta)m}\left[F_D\mathrm{sgn}(\dot{x}_u) + \left(1 + \frac{1}{2}R_m\right)m\ddot{x}_g + \left(1 + \frac{1}{2}R_m\right)\frac{\mathrm{mg}x_u}{2R}\right]. \quad (21)$$

When either θ_u or θ_l is equal to zero (Figure 1(c)), the horizontal acceleration of an ARI-SRB relative to ground when the roller is in motion within the arc rolling range d is obtained from the following equation:

$$\ddot{x}_u = \frac{-1}{(1 + 3/8R_m)m + b}\left[F_D\mathrm{sgn}(\dot{x}_u) + \left(1 + \frac{1}{2}R_m\right)m\ddot{x}_g + (1 + R_m)\frac{\mathrm{mg}x_u}{4R}\right],$$

$$= \frac{-1}{(1 + 3/8R_m + \beta)m}\left[F_D\mathrm{sgn}(\dot{x}_u) + \left(1 + \frac{1}{2}R_m\right)m\ddot{x}_g + (1 + R_m)\frac{\mathrm{mg}x_u}{4R}\right]. \quad (22)$$
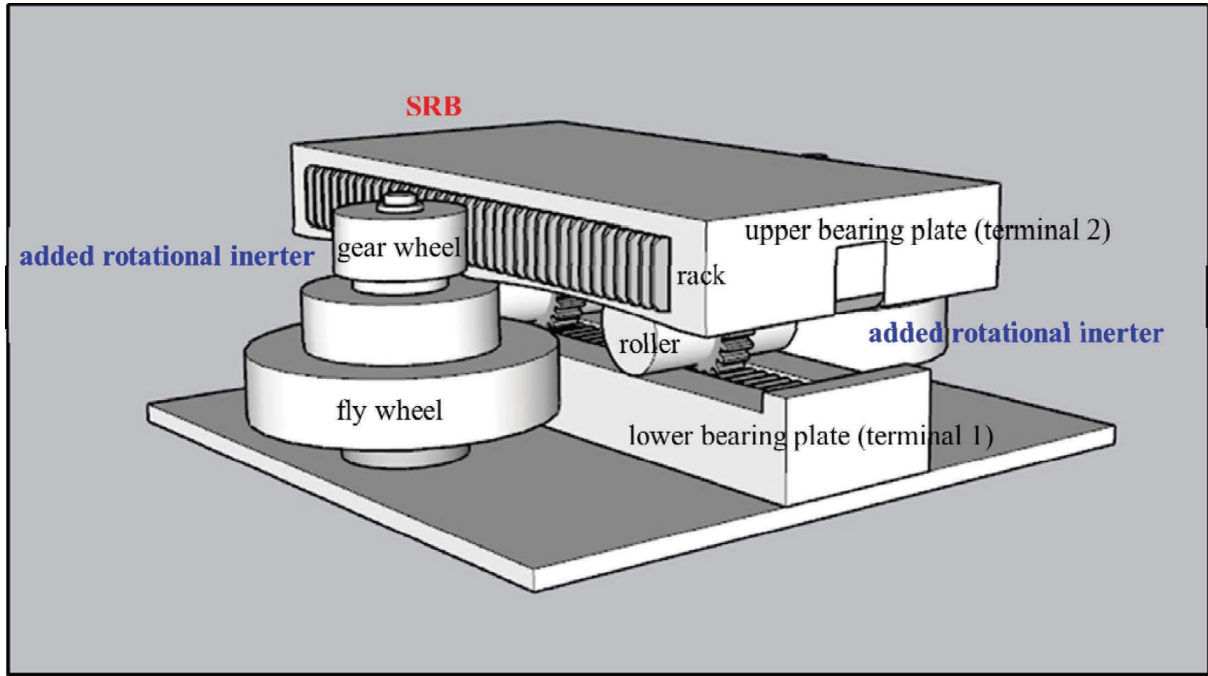
FIGURE 9: Illustration of the design mechanism of an ARI-SRB.

By comparing equations (20) to (22) with equations (13) to (15), it appears that consideration of the added rotational inerter of an ARI-SRB only contributes to the inertance represented in the denominator on the right-hand side of the equalities, which is much simpler analytically and numerically than consideration of the inherent rotational mass of an IRM-SRB. In addition, the value of b (or β) can be more easily and practically designed to be much larger than the value of $3R_m m/8$ (or $3R_m/8$) because of the inclusion of γ_m in (19). Considering the relative static state when the designed friction force is larger than the critical friction (obtained by setting $\ddot{x}_u = 0$ during numerical integration), the acceleration and displacement responses of IRM-SRBs and ARI-SRBs under external disturbances can be numerically analyzed based on the equations of motion given in equations (13) to (15) and equations (20) to (22), respectively.

3.2. Parametric Study of ARI-SRBs under Harmonic Excitation.
The harmonic excitation adopted here is the same as that described in Section 2.3.1. Details of the assumed parameters and the excitations considered for the parametric studies of ARI-SRBs are listed in Table 1.

3.2.1. First Parametric Study Results and Discussion.
The first parametric study of ARI-SRBs aimed to probe the variation of their peak acceleration and displacement responses with respect to β. The values set for all the parameters are identical to those described in Section 2.3.2, except that $R_m = 0.005$ was used for the IRM-SRB and ARI-SRB models for practical considerations and $A_g = 0.2$ g, 0.4 g, and 0.6 g were considered additionally. Precisely stated, unilateral periodic harmonic excitations with $T_g = 1$ s

and $A_g = 0.2$ g, 0.3 g, 0.4 g, and 0.6 g were used. Eleven sets of β in total, including one IRM-SRB model with $R_m = 0.005$ (equivalent to an ARI-SRB model with $\beta = 0$) and ten ARI-SRB models with $\beta = 0.05, 0.1, 0.15, 0.2, 0.25, 0.3, 0.35, 0.4,$ and 0.45, were considered. The 3-cycle hysteretic loops under harmonic excitation of the IRM-SRB model with $R_m = 0.005$ (obtained using equations (13) to (15)) and those of the ARI-SRB models with different values of β (obtained using equations (20) to (22)) are correspondingly represented by blue and red lines in Figures 10(a), 10(c), 10(e), and 10(g), for which the darker red color represents a larger value of β. To better understand the occurrence sequence of certain crucial relative displacement, relative velocity, and absolute acceleration responses, the corresponding absolute acceleration responses versus the relative velocity responses are presented in Figures 10(b), 10(d), 10(f), and 10(h), and the same symbol represents the same approximate time point during the numerical integration. Variations of the peak acceleration and displacement responses of the ARI-SRB models with respect to β are shown in Figures 11 and 12, respectively.

It appears that the larger the value of β, the more significant the effect of adding the rotational inerter, i.e., there was more significant mechanical clockwise rotation of the hysteresis loops. For each case of A_g, both peak acceleration and displacement responses could be reduced effectively with a smaller value of β, and the displacement responses were particularly noteworthy. The peak acceleration responses in the first and third quadrants, which occur when the roller is at the transition from the arc rolling range to the sloped rolling range, dominate the overall acceleration control performance. When the value of β becomes larger, the peak acceleration responses occurring at the peak displacement responses in the second and fourth quadrants
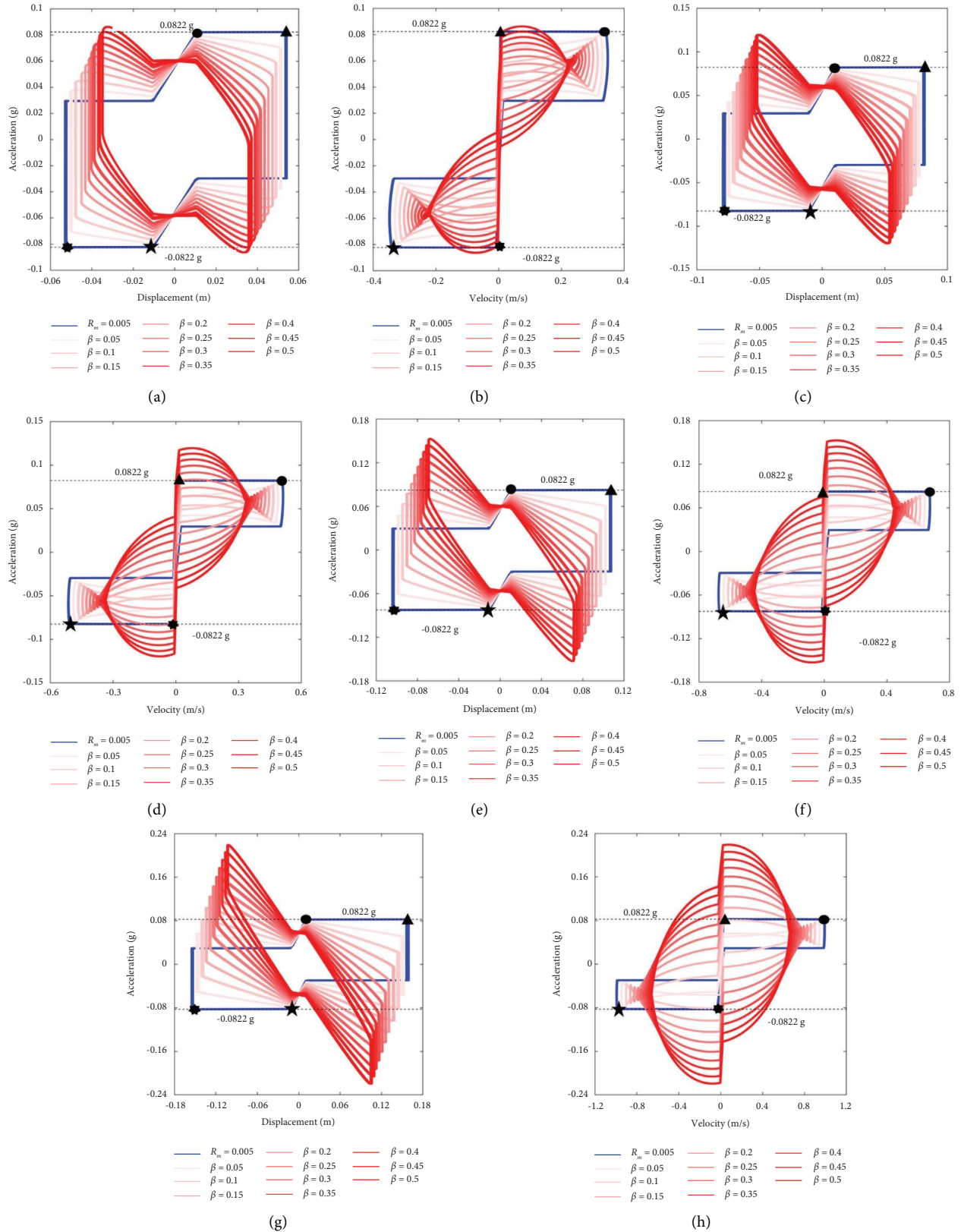
Figure 10: Hysteretic loops of ARI-SRB models with different β under harmonic excitations with $A_g = 0.2$ g, 0.3 g, 0.4 g, and 0.6 g and $T_g = 1$ s. (a) Absolute acceleration versus relative displacement ($A_g = 0.2$ g). (b) Absolute acceleration versus relative velocity ($A_g = 0.2$ g). (c) Absolute acceleration versus relative displacement ($A_g = 0.3$ g). (d) Absolute acceleration versus relative velocity ($A_g = 0.3$ g). (e) Absolute acceleration versus relative displacement ($A_g = 0.4$ g). (f) Absolute acceleration versus relative velocity ($A_g = 0.4$ g). (g) Absolute acceleration versus relative displacement ($A_g = 0.6$ g). (h) Absolute acceleration versus relative velocity ($A_g = 0.6$ g).
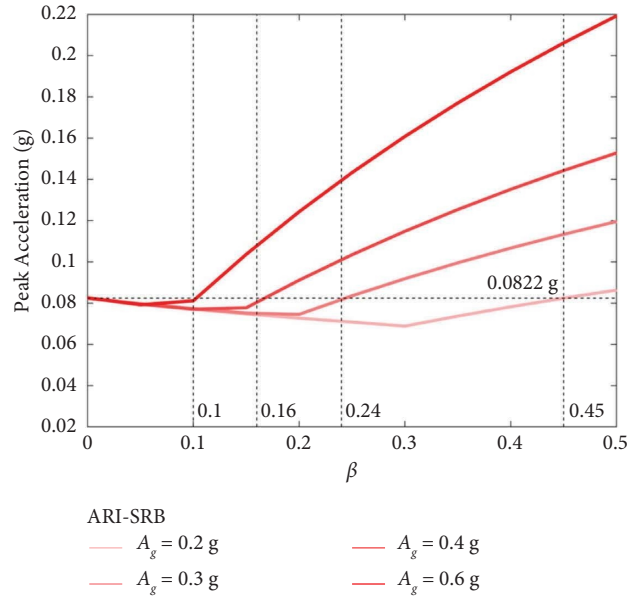
FIGURE 11: Variation of the peak acceleration responses of ARI-SRBs with respect to β under harmonic excitations with $A_g = 0.2$ g, 0.3 g, 0.4 g, and 0.6 g and $T_g = 1$ s.
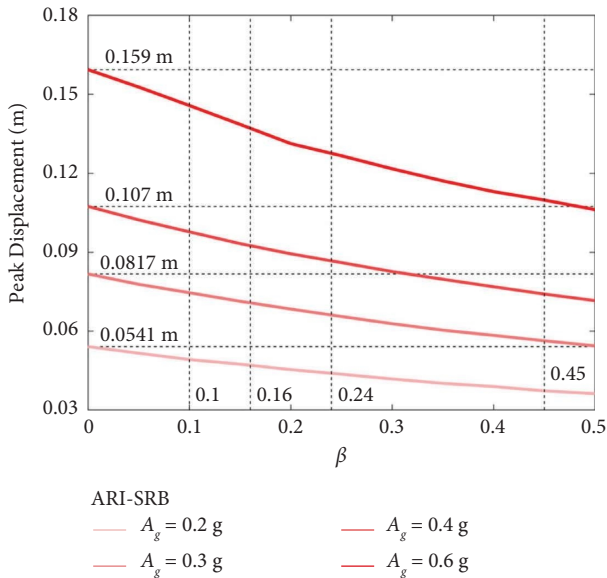

FIGURE 12: Variation of the peak displacement responses of ARI-SRBs with respect to β under harmonic excitations with $A_g = 0.2$ g, 0.3 g, 0.4 g, and 0.6 g and $T_g = 1$ s.

dominate the overall acceleration control performance and even exceed the horizontal transmitted constant acceleration designed for the SRB model (0.0822 g). The tendency for the corresponding reduction in displacement responses is still observed but is less significant. More importantly, when subjected to harmonic excitation with $A_g = 0.2$ g, 0.3 g, 0.4 g, and 0.6 g, the corresponding maximum design values of β (0.45, 0.24, 0.16, and 0.1) can be approximately determined from Figures 10(a) (or 10(b)), 10(c) (or 10(d)), 10(e) (or 10(f)), and 10(g) (or 10(h)), respectively, and those are presented in Figure 11, on the premise that the peak

acceleration response of the ARI-SRB model does not exceed the horizontal transmitted constant acceleration designed for the SRB model (0.0822 g).

3.2.2. Second Parametric Study Results and Discussion. The second parametric study of ARI-SRBs aimed to probe the variation of their peak acceleration and displacement responses with respect to A_g. The values set for all the parameters here are identical to those described in Section 3.2.1, except for adopting the four values of β determined in Section 3.2.1, i.e., 0.45, 0.24, 0.16, and 0.1, to guarantee that the ARI-SRB models would have smaller peak acceleration responses than 0.0822 g when $A_g = 0.2$ g, 0.3 g, 0.4 g, and 0.6 g (with respect to the β values). Unilateral periodic harmonic excitations with $T_g = 1$ s but with values of A_g varying from 0.1 g to 1 g with an increment of 0.1 g were used. The 3-cycle hysteretic loops under harmonic excitation of the IRM-SRB model with $R_m = 0.005$ and the ARI-SRB models with the four values of β correspondingly obtained using equations (13) to (15) and equations (20) to (22) are respectively represented as blue and red lines in Figure 13. Variations of the peak acceleration and displacement responses of the four ARI-SRB models with respect to A_g are shown in Figures 14 and 15, respectively.

Clearly, the peak displacement response of the ARI-SRB models is smaller than that of the IRM-SRB model with $R_m = 0.005$ under the same harmonic excitation, and it is almost linearly proportional to A_g. For each case of β and with a smaller value of A_g, the peak acceleration responses occurring in the first and third quadrants when the roller is at the transition from the arc rolling range to the sloped rolling range dominate the overall acceleration control performance, and they are slightly smaller than the horizontal transmitted constant acceleration designed for the
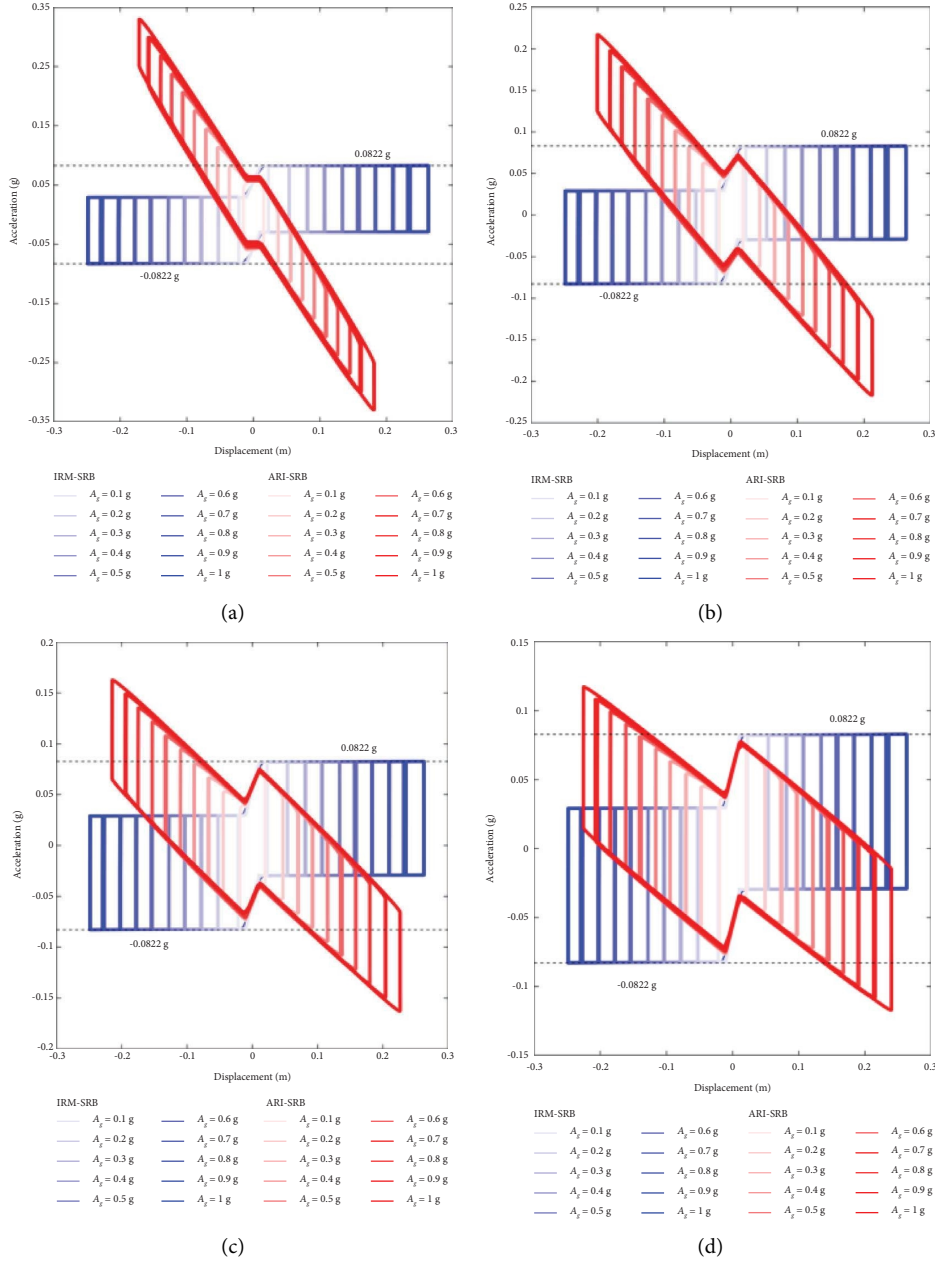
FIGURE 13: Hysteretic loops of ARI-SRB models with various β under harmonic excitations with A_g varying from 0.1 g to 1 g and $T_g = 1$ s. (a) $\beta = 0.45$ designed corresponding to $A_g = 0.2$ g. (b) $\beta = 0.24$ designed corresponding to $A_g = 0.3$ g. (c) $\beta = 0.16$ designed corresponding to $A_g = 0.4$ g. (d) $\beta = 0.1$ designed corresponding to $A_g = 0.6$ g.

SRB model (0.0822 g). When the value of A_g increases, the peak acceleration responses of the ARI-SRB models occur at the peak displacement responses in the second and fourth quadrants, and they begin to exceed 0.0822 g and are linearly proportional to A_g. It is worth noting that the peak acceleration responses of the ARI-SRB models designed with the four previously determined values of β, i.e., 0.45, 0.24, 0.16, and 0.1, are indeed smaller than 0.0822 g when subjected to the harmonic excitations with $A_g \leq 0.2$ g, 0.3 g, 0.4 g, and 0.6 g, respectively. This finding is very important and useful for the proposal of a design procedure for ARI-SRBs, which will be discussed in Section 4.

3.2.3. *Third Parametric Study Results and Discussion.* The third parametric study of ARI-SRBs aimed to probe the variation of their peak acceleration and displacement responses with respect to T_g. The values set for all the parameters here are identical to those described in Section 3.2.1, except for adopting the four values of β determined in Section 3.2.1, i.e., 0.45, 0.24, 0.16, and 0.1, to guarantee that the ARI-SRB models would have smaller peak acceleration responses than 0.0822 g when $A_g = 0.2$ g, 0.3 g, 0.4 g, and 0.6 g, with respect to the β values. Unilateral periodic harmonic excitations with the four values of A_g but with values of T_g varying from 0.1 s to 1 s with an increment of 0.1 s and
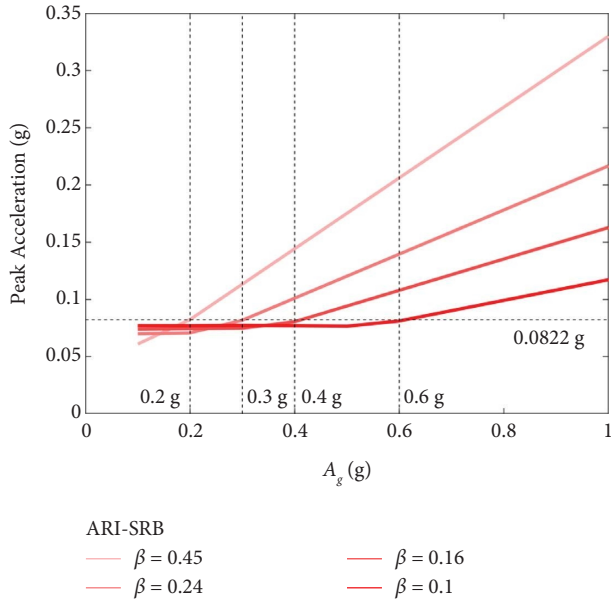
FIGURE 14: Variation of the peak acceleration responses of ARI-SRB models with various β with respect to A_g under harmonic excitations with $T_g = 1$ s.
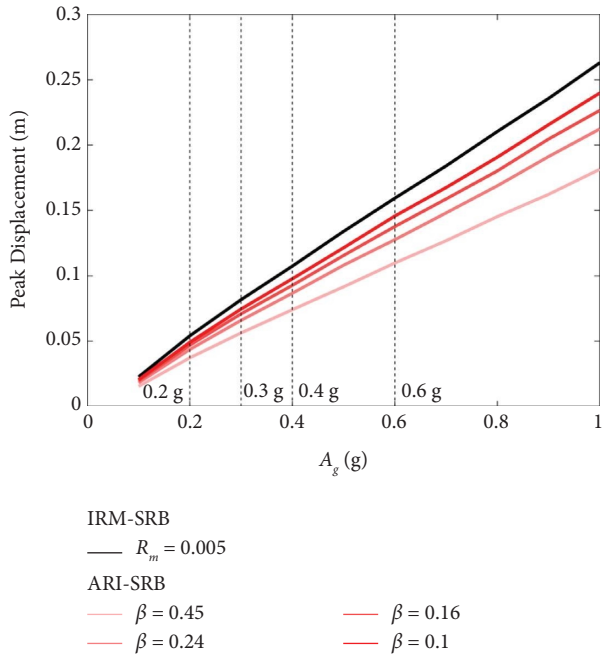

FIGURE 15: Variation of the peak displacement responses of ARI-SRB models with various β with respect to A_g under harmonic excitations with $T_g = 1$ s.

varying from 1 s to 10 s with an increment of 1 s were used. The 3-cycle hysteretic loops under harmonic excitation of the IRM-SRB model with $R_m = 0.005$ and the ARI-SRB models with the four values of β correspondingly obtained using equations (13) to (15) and equations (20) to (22) are presented in Figure 16. Variations of the peak acceleration and displacement responses of the four ARI-SRB models

with respect to T_g are shown in Figures 17 and 18, respectively.

It can be seen that for the ARI-SRB models, the smaller the value of T_g, the greater the clockwise rotation of the hysteresis loops. For each case of β, when the value of T_g is relatively small, the roller is still in motion within the arc rolling range. The peak acceleration responses at the peak displacement responses in the second and fourth quadrants, where the clockwise rotation of hysteresis loops becomes more significant, dominate the overall acceleration control performance and even exceed the horizontal transmitted constant acceleration designed for the SRB model (0.0822 g). This result when the roller is still in motion within the arc rolling range coincides with the previous observation of enlarged acceleration due to more significant inerter force generated at a higher frequency range [20, 21]. When equipped with an added rotational inerter with the aim of not exceeding the constant acceleration performance designed for the SRB model, the displacement responses can still be reduced. When the value of T_g becomes larger, both peak acceleration and displacement responses can be controlled very well. The peak acceleration responses in the second and fourth quadrants, which occur at the peak displacement responses, remain almost constant no matter how large T_g is (i.e., it is almost independent of T_g). This observation demonstrates again that the unique mechanical features of SRBs, namely possessing zero postyield stiffness, no fixed natural period, and offering maximum decoupling against external disturbances [4–7], still exist even considering the effect of β. Except for harmonic excitations with too small a T_g value, for which the roller is still in motion within the arc rolling range, the peak acceleration responses of the ARI-SRB models designed with the four previously determined values of β (0.45, 0.24, 0.16, and 0.1) can be controlled to be smaller than 0.0822 g when subjected to harmonic excitations with $A_g \leq 0.2$ g, 0.3 g, 0.4 g, and 0.6 g (corresponding to the β values). This finding is also very important and useful for the proposal of a design procedure for ARI-SRBs, which will be discussed in Section 4.

3.3. Hysteretic Behavior under Ground Motion

3.3.1. Ground Motion. Twenty-five sets of far-field ground motion records and 41 sets of pulse-like near-fault ground motion records [43] of past global earthquakes were adopted as horizontal acceleration inputs. To further understand and compare the merits and demerits of ARI-SRBs compared with IRM-SRBs (i.e., SRBs that appropriately consider roller mass but do not have an added rotational inerter), they were subjected to ground motions with different earthquake characteristics. These ground motion records were collected by the pacific earthquake engineering research center (PEER). The peak ground acceleration (PGA) and peak ground velocity (PGV) values of the far-field ground motion records ranged from 0.152 g to 0.621 g and from 0.208 m/s to 0.704 m/s, respectively; the PGA and PGV values of the
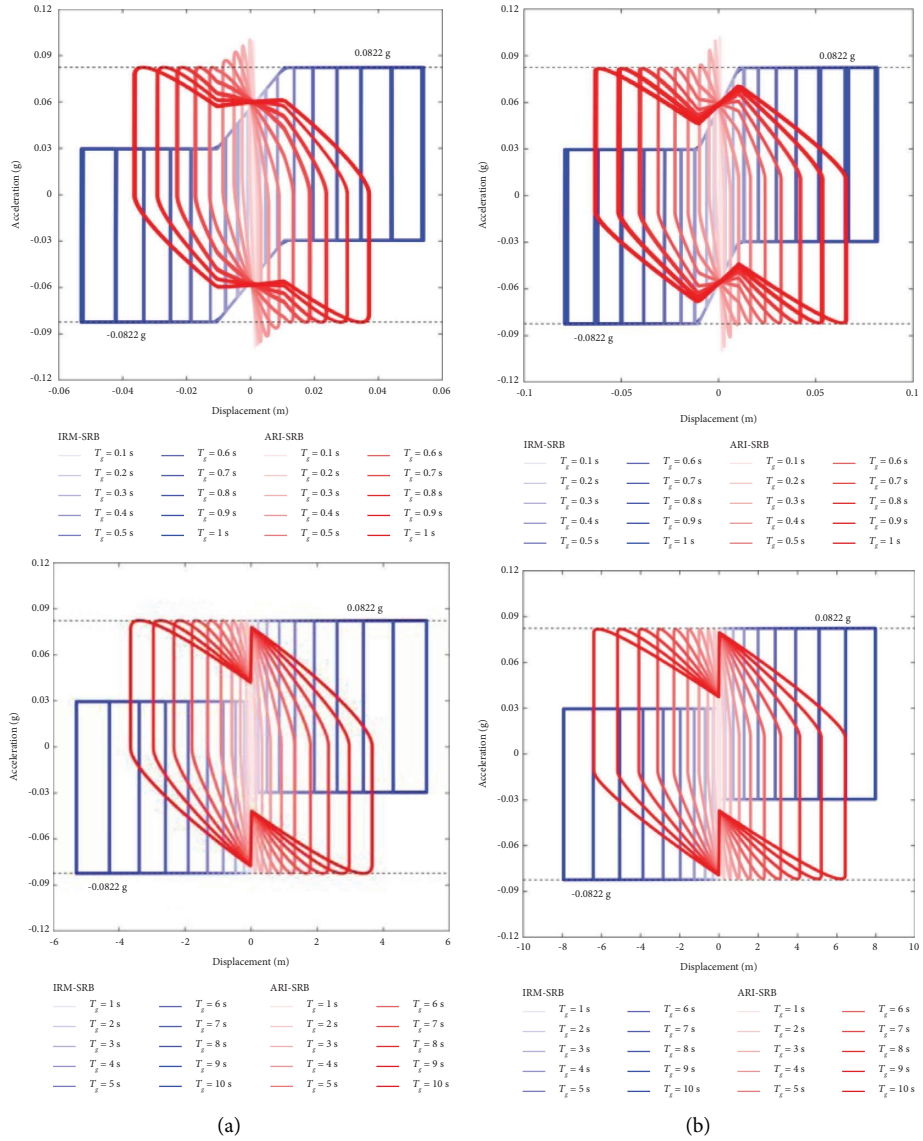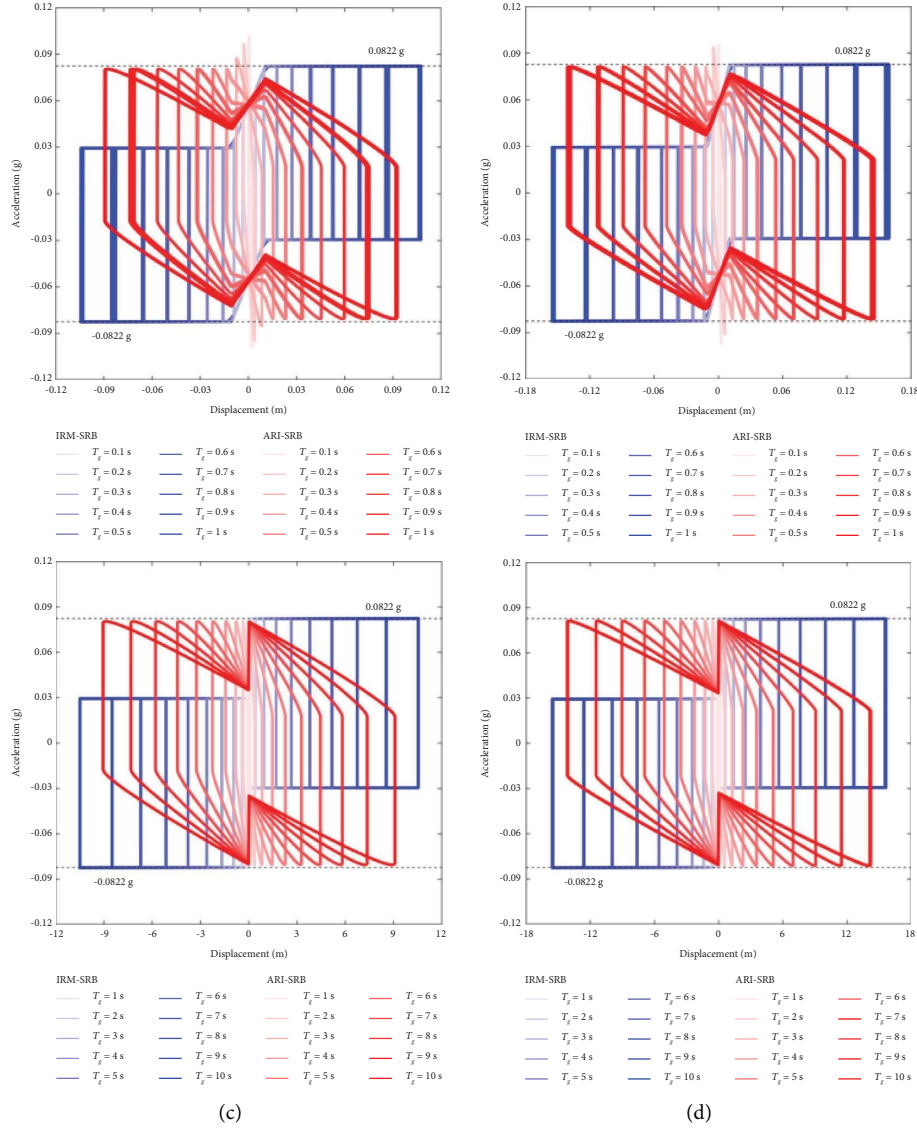
FIGURE 16: Continued.

Figure 16: Hysteretic loops of ARI-SRB models with various β under harmonic excitations with various A_g and T_g. (a) $\beta = 0.45$ designed corresponding to $A_g = 0.2$ g. (b) $\beta = 0.24$ designed corresponding to $A_g = 0.3$ g. (c) $\beta = 0.16$ designed corresponding to $A_g = 0.4$ g. (d) $\beta = 0.1$ designed corresponding to $A_g = 0.6$ g.

pulse-like near-fault ground motion records ranged from 0.144 g to 1.129 g and from 0.440 m/s to 1.479 m/s, respectively. The basic information about these ground motion records, including the earthquake, year of occurrence, station name, PGA, and PGV, is summarized in Tables 2 and 3. Their acceleration response spectra are shown in Figure 19(a), which shows that the adopted ground motion records possess a wide range of period content. The ground motion records are denoted by the corresponding number (No.) listed in the tables for simplicity.

3.3.2. Comparison between ARI-SRBs and IRM-SRBs.
Two indices, R_a and R_d, are defined here to quantitatively judge whether ARI-SRBs perform better than IRM-SRBs when subjected to ground motion, as described by the following equations , respectively:

$$R_a = \left(\frac{A_{\text{ARI–SRB}}}{A_{\text{IRM–SRB}}} - 1 \right) \times 100\%, \tag{23}$$

$$R_d = \left(1 - \frac{D_{\text{ARI–SRB}}}{D_{\text{IRM–SRB}}} \right) \times 100\%, \tag{24}$$

where $A_{\text{ARI-SRB}}$ and $D_{\text{ARI-SRB}}$ are the peak acceleration and displacement responses of an ARI-SRB, respectively. If R_a is negative and R_d is positive, this means that ARI-SRBs perform better than IRM-SRBs at controlling both acceleration and displacement responses.

Let $m = 1$ ton, $\theta_u = 0$ degrees, $\theta_l = 3$ degrees, $\mu^* = 0.0561$ (i.e., $F_D = 550$ N), $R = 0.1$ m, $d = 0.0105$ m, $R_m = 0.005$ (appropriately assuming the roller mass to be equal to 0.005 times the total mass of the protected object and upper bearing plate), and $\beta = 0.45$, 0.24, 0.16, and 0.1 for the four
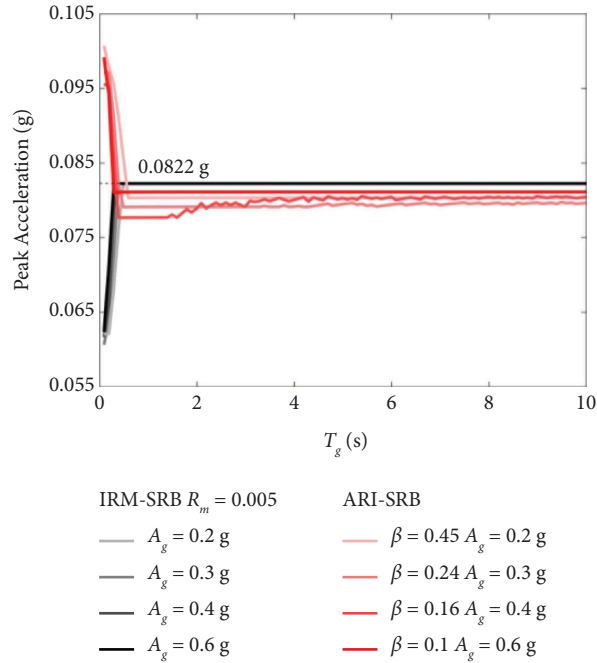
FIGURE 17: Variation of the peak acceleration responses of ARI-SRB models with various β with respect to T_g under harmonic excitations with corresponding A_g.
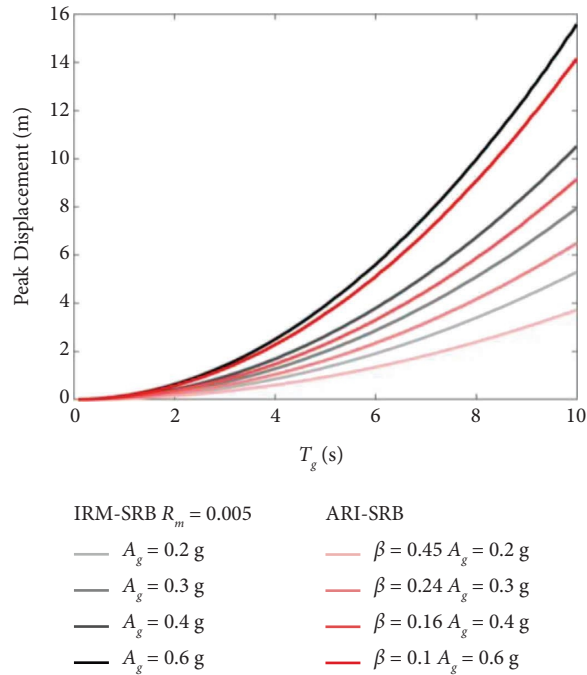

FIGURE 18: Variation of the peak displacement responses of ARI-SRB models with various β with respect to T_g under harmonic excitations with corresponding A_g.

ARI-SRB models, and $\beta = 0$ for the IRM-SRB model with $R_m = 0.005$. Note that the peak displacement responses of the ARI-SRB and IRM-SRB models under all the ground motion records listed in Tables 2 and 3 exceed the design value of d, i.e., the roller will move in the sloped rolling range throughout all the ground motion records. Under the far-

field ground motion listed in Table 2, calculations of R_a and R_d for the ARI-SRB models of the four values of β are presented in Figure 20. Likewise, calculations of R_a and R_d for the four ARI-SRB models under the pulse-like near-fault ground motion listed in Table 3 are presented in Figure 21. To provide for a better comparison, R_a and R_d versus No.,

TABLE 2: Far-field ground motion records.

Nos.	Earthquakes	Years	Station names	PGA (g)	PGV (m/s)
FF-1	EI Centro	1940	American imperial valley	0.281	0.309
FF-2	American Imperial Valley	1979	Delta (352)	0.350	0.330
FF-3	American Superstition Hills	1987	Poe Road (270)	0.475	0.412
FF-4	American Loma Prieta	1989	Gilroy Array #3 (000)	0.559	0.363
FF-5			Capitola (090)	0.439	0.296
FF-6	Iran Manjil	1990	Abbar (L)	0.515	0.425
FF-7	American Landers	1992	Yermo Fire (360)	0.152	0.291
FF-8	American Northridge	1994	Beverly Hills-12520 Mulhol (035)	0.621	0.288
FF-9			Canyon Country (270)	0.472	0.411
FF-10			LA-Saturn St (020)	0.468	0.372
FF-11			LA-Hollywood Stor FF (360)	0.358	0.274
FF-12	Japan Kobe	1995	Nishi-Akashi (000)	0.483	0.468
FF-13			Tadoka (000)	0.296	0.245
FF-14			Kakogwa (000)	0.240	0.208
FF-15			Shin-Osaka (090)	0.233	0.218
FF-16			MRG (000)	0.214	0.270
FF-17			Fukushima (000)	0.185	0.314
FF-18			Yae (000)	0.158	0.212
FF-19	Turkey Kocaeli	1999	Duzce (270)	0.364	0.577
FF-20	Taiwan Chi-Chi	1999	TCU074 (EW)	0.597	0.704
FF-21			TCU045 (NS)	0.522	0.460
FF-22			TCU088 (EW)	0.519	0.137
FF-23			TCU047 (NS)	0.407	0.333
FF-24			NST (NS)	0.399	0.329
FF-25			TCU089 (EW)	0.355	0.508

TABLE 3: Pulse-like near-fault ground motion records.

Nos.	Earthquakes	Years	Station names	PGA (g)	PGV (m/s)
NF-1	American San Fernanado	1971	Pacoima Dam (upper left abut) (164)	1.129	1.144
NF-2	American Superstition	1987	Parachute Test Site (225)	0.429	1.342
NF-3	American Lexington Dam	1989	LosGatos (090)	0.409	0.957
NF-4	American Cape Mendocino	1992	Petrolia (090)	0.605	0.885
NF-5	Turkey Erzincan	1992	Erzincan (NS)	0.385	1.071
NF-6	American Northridge	1994	Pacoima Dam (upper left) (194)	0.989	1.033
NF-7			Rinaldi (228)	0.869	1.479
NF-8			Sylmar-Converter Sta East (011)	0.851	1.209
NF-9			Sylmar-Olive View Med FF (360)	0.798	1.293
NF-10			Sylmar-Converter Sta (052)	0.617	1.162
NF-11			Jensen Filter Plant Generator building (022)	0.569	0.761
NF-12	Taiwan Chi-Chi	1999	TCU067 (EW)	0.498	0.983
NF-13			CHY101 (NS)	0.398	1.073
NF-14			TCU052 (EW)	0.357	1.746
NF-15			CHY101 (EW)	0.340	0.672
NF-16			TCU075 (EW)	0.330	1.161
NF-17			TCU102 (EW)	0.310	0.874
NF-18			CHY024 (EW)	0.282	0.529
NF-19			TCU063 (EW)	0.183	0.440
NF-20			TCU102 (NS)	0.172	0.713
NF-21			TCU128 (NS)	0.166	0.626
NF-22			TCU128 (EW)	0.144	0.642
NF-23	Turkey Kocaeli	1999	Yarimca (150)	0.320	0.719
NF-24			Yarimca (060)	0.226	0.697
NF-25	New Zealand Darfield	2010	HORC (S72E)	0.472	0.698
NF-26	Taiwan Meinong	2016	CHY089 (NS)	0.288	0.577

Table 3: Continued.

| Nos.	Earthquakes	Years	Station names	PGA (g)	PGV (m/s)
NF-27			HWA019 (EW)	0.411	1.384
NF-28			HWA008 (NS)	0.343	0.861
NF-29			MND016 (EW)	0.306	1.336
NF-30			HWA007 (EW)	0.295	1.034
NF-31			HWA012 (EW)	0.285	0.866
NF-32			HWA063 (NS)	0.258	0.997
NF-33			HWA028 (NS)	0.258	0.517
NF-34	Taiwan Hualien	2018	HWA009 (EW)	0.255	1.104
NF-35			HWA008 (EW)	0.235	0.992
NF-36			HWA 062 (EW)	0.213	0.956
NF-37			TRB042 (EW)	0.208	0.656
NF-38			HWA062 (NS)	0.207	0.764
NF-39			HWA011 (NS)	0.203	0.871
NF-40			HWA050 (NS)	0.202	0.763
NF-41			TRB042 (NS)	0.190	0.826

(a)

(b)
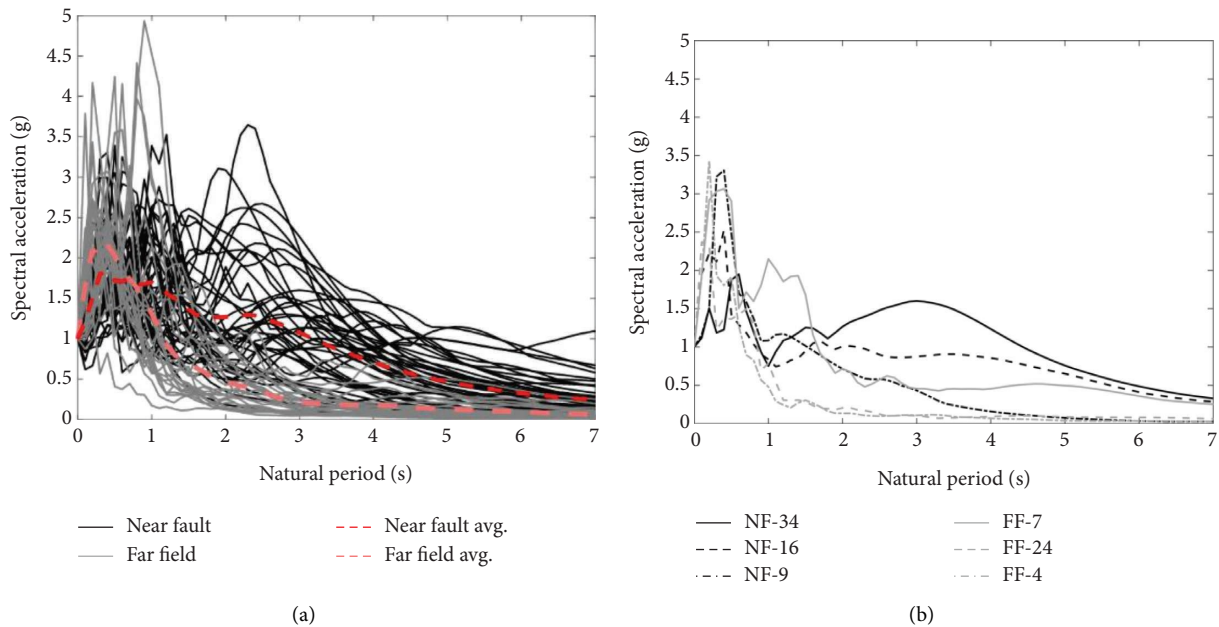
Figure 19: Acceleration response spectra of ground motion records. (a) All ground motion records. (b) FF-7, FF-24, FF-4, NF-34, NF-16, and NF-9.

PGA, and PGV are provided in these figures. It can be seen that all the calculations of R_a are positive except when $\beta = 0.24$, 0.16, and 0.1 under FF-7, for which the hysteresis loops of the four ARI-SRB models and the IRM-SRB model are presented in Figure 22(a). All the calculations of R_d are positive and quite steady under all the ground motion records for each ARI-SRB model. With $\beta = 0.45$, 0.24, 0.16, and 0.1, the approximate averages of R_d (i.e., the displacement reduction) under the far-field (and pulse-like near-fault) ground motion records are correspondingly 30.1%, 18.5%, 13.1%, and 9.5% (and 28.0%, 17.9%, 12.5%, and 8.6%), as presented in Figure 20(e) (and Figure 21(e)). This qualitatively indicates that adopting an added rotational inerter for an SRB is definitely beneficial for reducing peak displacement responses, regardless of whether it is subjected to far-field or pulse-like near-fault ground motion. Increasing the

value of β (the inertance) is helpful for displacement control performance although it sacrifices acceleration control performance, and vice versa. In addition to Figure 22(a), Figures 22(b)–22(f) correspondingly present the hysteresis loops of the four ARI-SRB models and the IRM-SRB model under FF-24, FF-4, NF-34, NF-16, and NF-9 for better understanding and comparison. The acceleration response spectra of FF-7, FF-24, FF-4, NF-34, NF-16, and NF-9 are presented in Figure 19(b). The PGA values of the ground motion chosen for Figures 22(a)–22(c) are approximately equal to or less than 0.2 g, 0.4 g, and 0.6 g, respectively, and the PGV values of the ground motion chosen for Figures 22(d)–22(f) are larger than 1 m/s. It is demonstrated again through comparison of Figures 22(a)–22(f) that when the ground motion has more low-period content (e.g., at natural periods shorter than 0.5 s for FF-4 or NF-9, as shown
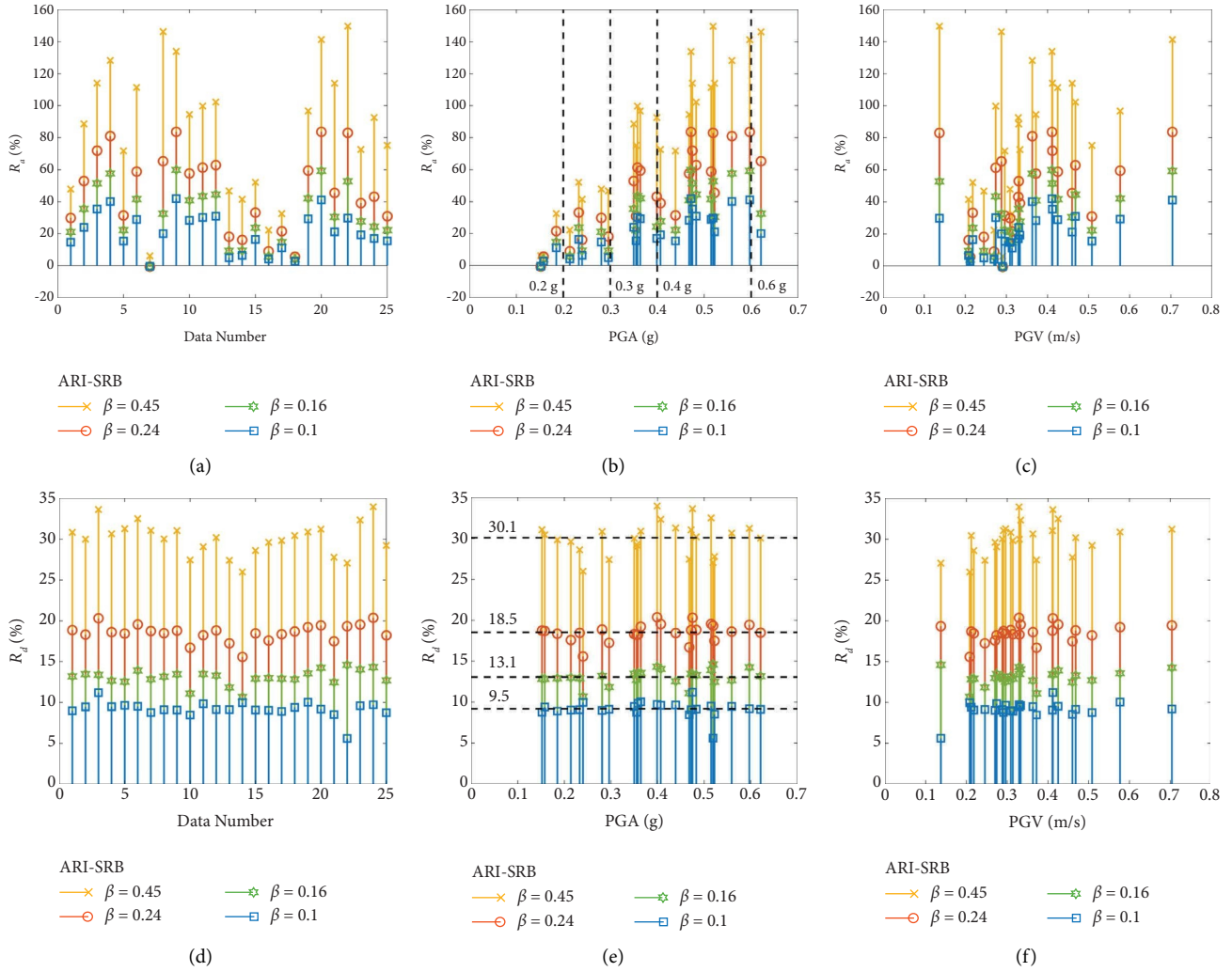
FIGURE 20: R_a and R_d for ARI-SRB models with $\beta = 0.45$, 0.24, 0.16, and 0.1 under far-field ground motion. (a) R_a (ordered by No.). (b) R_a (ordered by PGA). (c) R_a (ordered by PGV). (d) R_d (ordered by No.). (e) R_d (ordered by PGA). (f) R_d (ordered by PGV).

in Figure 19(b)), more acceleration amplification arising from more significant inerter force generated is observable, which coincides with the parametric analysis results under harmonic excitation and past relevant studies [20, 21].

Figures 20(b) and 21(b) further show that, in general, the larger the value of PGA, the larger the calculated R_a. This is particularly evident when subjected to pulse-like near-fault ground motion. The dotted lines plotted in Figures 20(b) and 21(b) represent PGA = 0.2 g, 0.3 g, 0.4 g, and 0.6 g, which are the acceleration targets (i.e., the four A_g values of the harmonic excitations) used for determining the four values of β to design the ARI-SRB models, as detailed in Section 3.2.1. Nearly the same tendency as that observed in Sections 3.2.2 and 3.2.3 was observed. The existence of quantitative differences is reasonable due to the fact that ground motion is unlike harmonic excitation which only has a fixed frequency and that the dynamic responses when subjected to ground motion are not steady-state responses completely. The ARI-SRB model whose β value was determined using harmonic excitation with a specific value of A_g generally

exhibited slightly worse but still acceptable acceleration control performance compared with the IRM-SRB model with $R_m = 0.005$ when subjected to ground motion whose PGA value is equal to or less than A_g. Quantitatively speaking, when the PGA values are equal to or less than acceleration targets of 0.2 g, 0.3 g, 0.4 g, and 0.6 g, the corresponding ARI-SRB models have larger peak acceleration responses than the IRM-SRB model with $R_m = 0.005$ by less than 50% in general and by 15.1%, 16.6%, 19.7%, and 21.2% on average, respectively. The acceleration control performance of the ARI-SRB model under pulse-like near-fault ground motion may be slightly inferior to that under far-field ground motion, which is rational because pulse-like near-fault ground motion has a significant velocity pulse. Quantitatively speaking, when the PGA values are equal to or less than acceleration targets of 0.2 g, 0.3 g, 0.4 g, and 0.6 g, the corresponding ARI-SRB models have larger peak acceleration responses than the IRM-SRB model with $R_m = 0.005$ by 29.5%, 25.8%, 22.2%, and 18.4% on average, respectively. These phenomena can be more clearly seen in
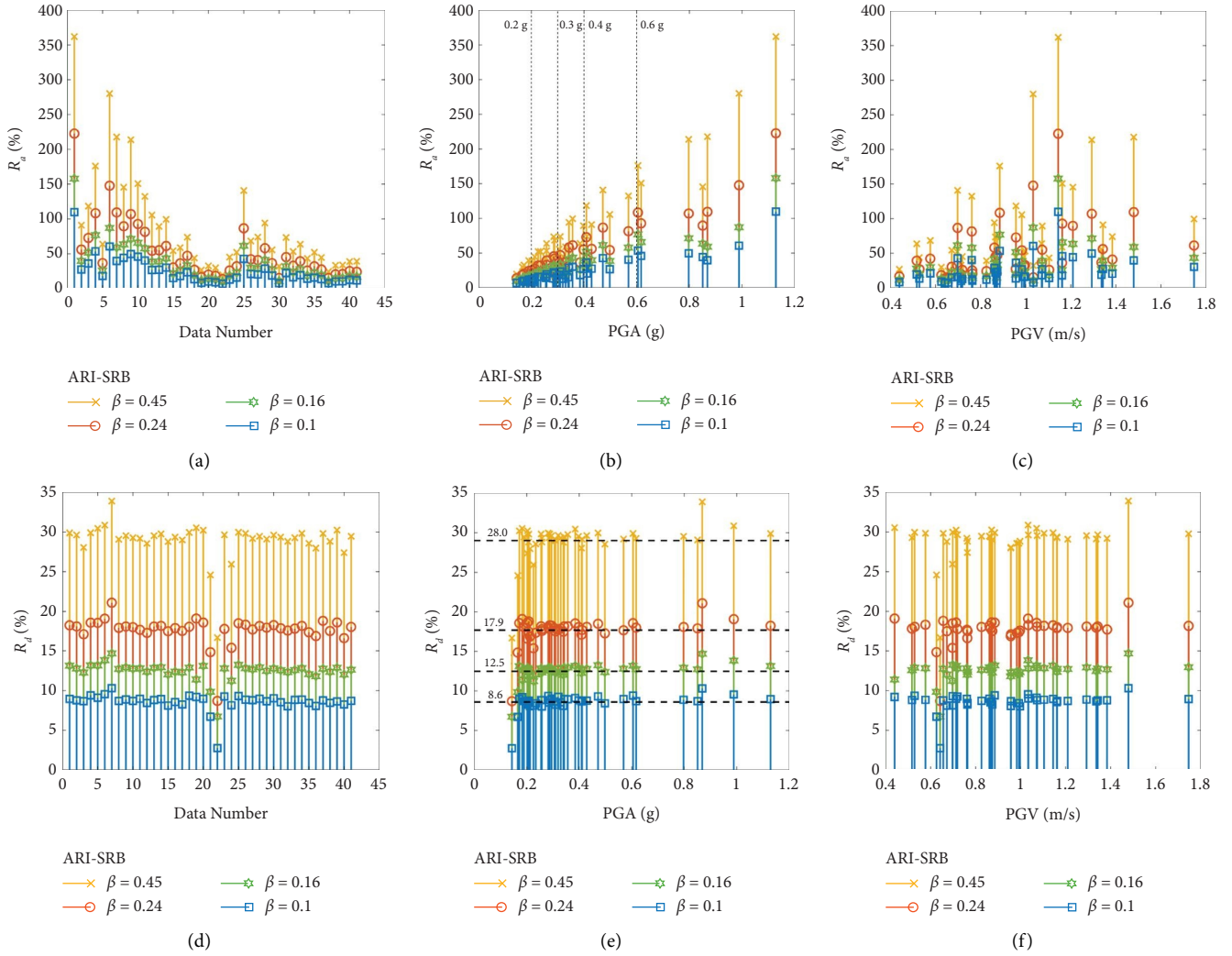
FIGURE 21: R_a and R_d for ARI-SRB models with $\beta = 0.45$, 0.24, 0.16, and 0.1 under pulse-like near-fault ground motion. (a) R_a (ordered by No.). (b) R_a (ordered by PGA). (c) R_a (ordered by PGV). (d) R_d (ordered by No.). (e) R_d (ordered by PGA). (f) R_d (ordered by PGV).

Figure 23, which contains all the calculations of R_a under all the ground motions in order of PGA magnitude (the solid and dotted lines represent the calculations under the far-field and pulse-like near-fault ground motion records, respectively). For all the ground motions, the averages of R_a for the ARI-SRB models with $\beta = 0.45$, 0.24, 0.16, and 0.1 when the PGA values are correspondingly equal to or less than acceleration targets of 0.2 g, 0.3 g, 0.4 g, and 0.6 g are 24.9%, 23.1%, 21.4%, and 19.6%, respectively.

4. Acceleration-Based Design Procedure for ARI-SRBs

Based on the parametric analysis results of the ARI-SRBs described in Section 3.2 and the seismic responses of the ARI-SRBs described in Section 3.3, a simple, practical, and acceleration-based procedure for designing ARI-SRBs is proposed. First, the seismic demand in terms of PGA and the horizontal transmitted constant acceleration of SRBs are to be determined. The design parameters of an SRB, including

sloping angles and friction damping force, can then be determined accordingly. The maximum value of β for an ARI-SRB can then be determined based on ensuring that the peak acceleration response under harmonic excitation with an acceleration amplitude equal to the initially determined PGA value is less than the designed constant acceleration transmitted by the SRB. Note that the harmonic excitation period can be chosen arbitrarily as long as it is not too small, which would enlarge the acceleration of the ARI-SRBs because the roller of the SRB would still be in motion within the arc rolling range. In other words, very short excitation periods and SRB rollers still moving within the arc rolling range are excluded from this discussion, which are equivalent to circumstances in which the seismic demand usually has less damage potential and the seismic isolation system is not yet fully activated. Finally, nonlinear response history analysis using ground motion is conducted to verify or adjust the inertance factor of the ARI-SRB as required. The flowchart of the proposed acceleration-based design procedure for ARI-SRBs is presented in Figure 24.
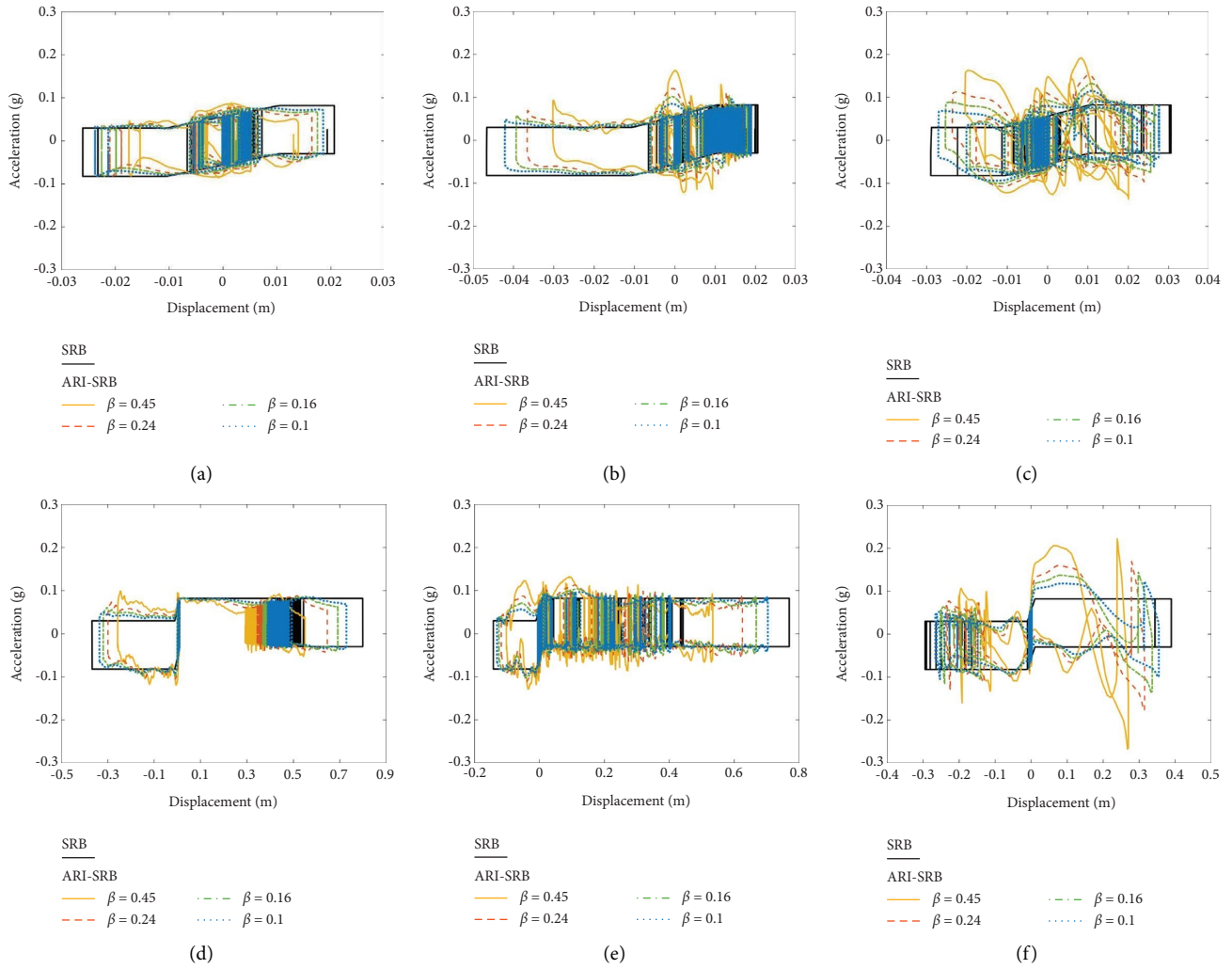
Figure 22: Hysteresis loops of ARI-SRB and IRM-SRB models under various ground motion records. (a) FF-7 (PGA = 0.152 g). (b) FF-24 (PGA = 0.399 g). (c) FF-4 (PGA = 0.559 g). (d) NF-34 (PGV = 1.104 m/s). (e) NF-16 (PGV = 1.161 m/s). (f) NF-9 (PGV = 1.293 m/s).
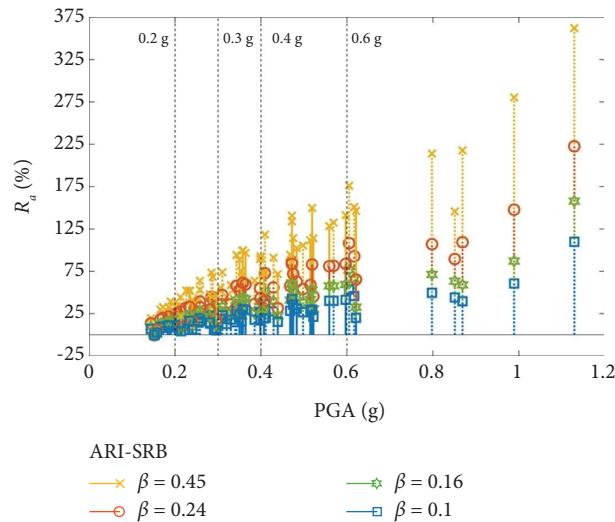

Figure 23: R_a for ARI-SRB models with β = 0.45, 0.24, 0.16, and 0.1 under all ground motion records.

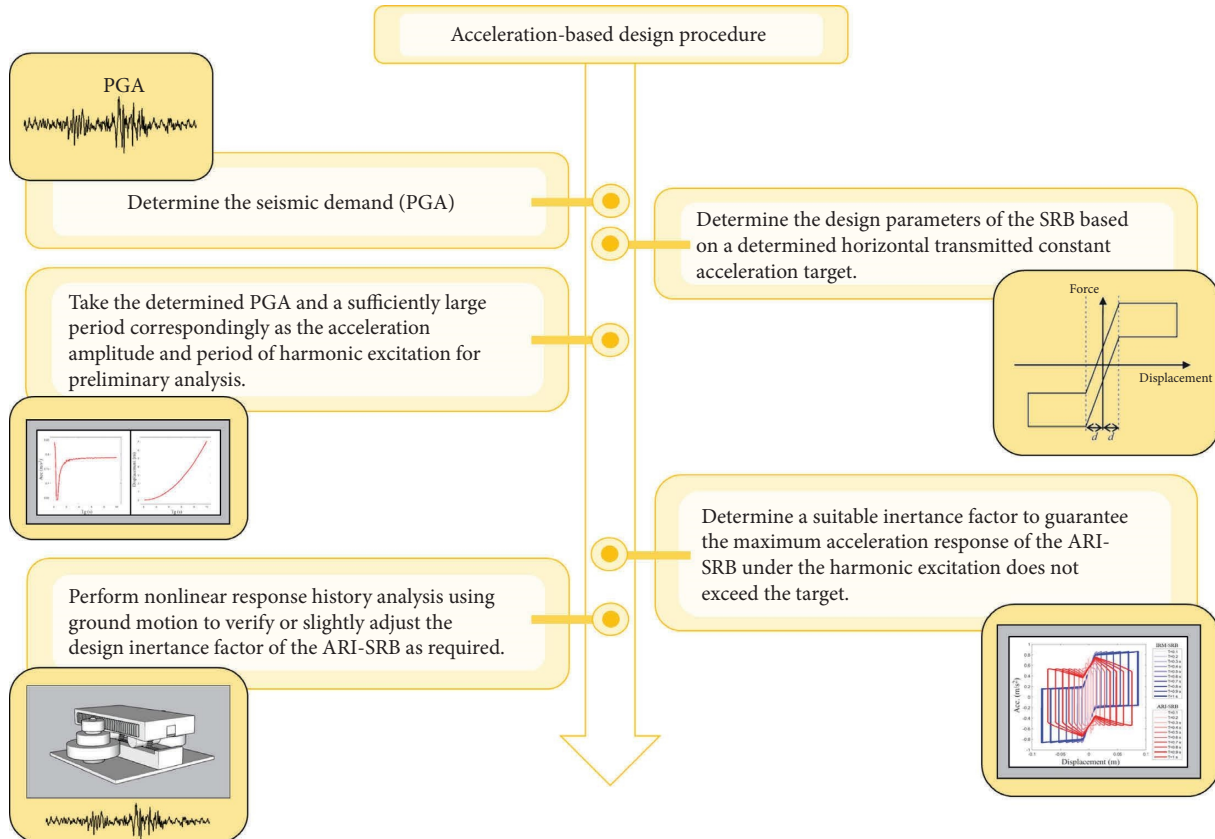Figure 24: Flowchart of the acceleration-based design procedure proposed for ARI-SRBs.

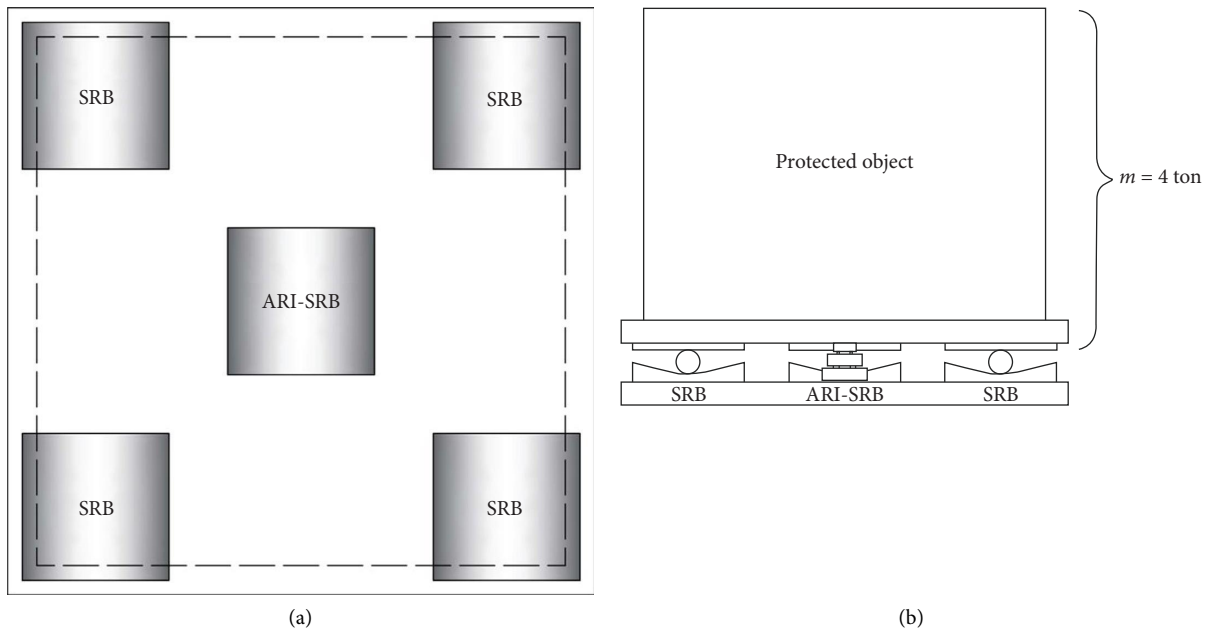(a)   (b)

Figure 25: Illustration of the design example. (a) Plane view. (b) Lateral view.

A simple design example of the combination of SRBs and ARI-SRBs in accordance with the proposed design procedure is provided as follows. The total mass (m given in equation (10)) is assumed to 4 ton, which is sustained by a seismic isolation system composed of four SRBs and one ARI-SRB, as illustrated in Figure 25. The PGA demand ($\ddot{x}_g$ given in (10)) is set to 0.4 g and the horizontal transmitted constant acceleration target of the SRBs ($\ddot{x}_u + \ddot{x}_g$ given in (10)) is controlled as 0.1 g. Then, the sloping angles (θ_u and θ_l given in (10)) and the friction damping force (F_D given in (10)) designed for the four SRBs can be calculated as per (10). The calculations of θ_u and θ_l for each SRB and the ARI-SRB are 0 and 5 degrees, respectively, and the calculation of F_D for each SRB is 550 N. By performing nonlinear response analysis on the seismic isolation system using harmonic excitation with an acceleration amplitude equal to the determined PGA demand (0.4 g) and a sufficiently larger period (e.g., 0.5 s), the design inertance factor (β given in equations (20) to (22)) of the ARI-SRB can be obtained as 0.295 to ensure that the maximum acceleration response under the harmonic excitation does not exceed the control target (0.1 g). Finally, nonlinear response history analysis using FF-7 and NF-34 given in Table 2, whose PGA values are equal to or less than the determined PGA demand (0.4 g), is conducted to adjust the inertance factor of the ARI-SRB. Under FF-7 and NF-34, the analyzed maximum acceleration responses are correspondingly 0.1 g and 0.12 g, which are almost comparable to the control target (0.1 g).

5. Conclusions

Sloped rolling-type bearings (SRBs) which consider the inherent rotational mass of the roller (IRM-SRBs) and IRM-SRBs with an added external rotational inerter (ARI-SRBs) were analytically and numerically investigated under harmonic excitation and ground motion. The following conclusions are drawn:

(1) Different equations of motion for IRM-SRBs and ARI-SRBs were theoretically deduced, which has not been done in previous studies. The derivations indicate that the rotational motion of the cylindrical roller of existing SRBs contributes to the inertial and restoring forces, whereas the added rotational inerter only contributes to inertance. The parametric study under harmonic excitation further demonstrated that the effects of the inertance factor, target acceleration amplitude, and harmonic excitation period (β, A_g, and T_g) on the mechanical behavior of ARI-SRBs in terms of hysteresis, acceleration, and displacement are different from those of mass ratio (R_m), A_g, and T_g on the mechanical behavior of IRM-SRBs. SRBs that appropriately consider inherent rotational mass have relatively enlarged acceleration and displacement responses. Therefore, adopting the IRM-SRB model proposed in this study can provide more accurate and conservative design results, especially when the roller mass of the SRB is not negligible compared with the total mass of the protected object and upper bearing plate.

(2) For ARI-SRBs, the parametric study under harmonic excitation showed that the peak displacement response is proportional to A_g and T_g and inversely proportional to β. The peak acceleration responses that occur in the first and third quadrants and those in the second and fourth quadrants of hysteresis curves dominate the overall acceleration control performance for smaller and larger values of β or A_g, respectively. For the former case, the peak acceleration responses are slightly smaller than the constant acceleration designed for SRBs that do not consider inherent rotational mass when the roller is at the transition point from the arc rolling range to the sloped rolling range, whereas for the latter case, they become larger and occur at the peak displacement responses because of the more significant clockwise rotation of the hysteresis loops. For both smaller and larger T_g, the peak acceleration responses occurring in the second and fourth quadrants always dominate the overall acceleration control performance. For the former case, the peak acceleration responses appear to be larger than the constant acceleration designed for SRBs that do not consider inherent rotational mass when the roller is still in motion within the arc rolling range, whereas for the latter case, they decrease but are almost the same and occur at the peak displacement responses. With increasing T_g, the peak acceleration responses that occur in the second and fourth quadrants are no longer enlarged, which implies that the peak acceleration responses of ARI-SRBs are less dependent on having a sufficiently large harmonic excitation period (or on having the roller in motion within the sloped rolling range).

(3) When subjected to ground motion, regardless of whether it is far-field or pulse-like near-fault motion, the same tendency as that observed for ARI-SRBs under harmonic excitation was observed. The larger the peak ground acceleration (PGA), the larger the peak acceleration response. The peak displacement responses of ARI-SRBs compared with IRM-SRBs can be effectively reduced and almost steadily controlled. Increasing inertance is helpful for reducing displacement, although it sacrifices acceleration control performance, and vice versa. Most importantly, ARI-SRBs have slightly worse but still acceptable acceleration control performance compared with IRM-SRBs when subjected to ground motion whose PGA value is equal to or less than the value of A_g chosen to determine the value of β.

(4) Based on the parametric and numerical analysis results, a simple and practical acceleration-based procedure was proposed for designing ARI-SRBs without considering whether the excitation period is too small or whether the roller is still within the arc rolling range.

(5) After the feasibility and efficacy of ARI-SRBs have been numerically demonstrated in this study, further relevant experimental verification will be performed in future studies.

Data Availability

The data used to support the findings of this study are available from the corresponding author upon reasonable request.

Conflicts of Interest

The authors declare that they have no conflicts of interest.

Acknowledgments

References

[1] P. S. Harvey and K. C. Kelly, "A review of rolling-type seismic isolation: historical development and future directions," *Engineering Structures*, vol. 125, pp. 521–531, 2016.

[2] M. H. Tsai, S. Y. Wu, K. C. Chang, and G. C. Lee, "Shaking table tests of a scaled bridge model with rolling type seismic isolation bearings," *Engineering Structures*, vol. 29, no. 5, pp. 694–702, 2007.

[3] G. C. Lee, Y. C. Ou, T. Niu, J. Song, and Z. Liang, "Characterization of a roller seismic isolation bearing with supplemental energy dissipation for highway bridges," *Journal of Structural Engineering*, vol. 136, no. 5, pp. 502–510, 2010.

[4] S. J. Wang, J. S. Hwang, K. C. Chang et al., "Sloped multi-roller isolation devices for seismic protection of equipment and facilities," *Earthquake Engineering & Structural Dynamics*, vol. 43, no. 10, pp. 1443–1461, 2014.

[5] S. J. Wang, C. H. Yu, W. C. Lin, J. S. Hwang, and K. C. Chang, "A generalized analytical model for sloped rolling-type seismic isolators," *Engineering Structures*, vol. 138, pp. 434–446, 2017.

[6] S. J. Wang, C. H. Yu, C. Y. Cho, and J. S. Hwang, "Effects of design and seismic parameters on horizontal displacement responses of sloped rolling-type seismic isolators," *Structural Control and Health Monitoring*, vol. 26, no. 5, p. 2342, 2019.

[7] S. J. Wang, Y. L. Sung, C. Y. Yang, W. C. Lin, and C. H. Yu, "Control performances of friction pendulum and sloped rolling-type bearings designed with single parameters," *Applied Sciences*, vol. 10, no. 20, p. 7200, 2020.

[8] S. J. Wang and Y. L. Sung, "Control performance of sloped rolling-type isolators designed with stepwise variable parameters," *Smart Structures and Systems*, vol. 27, no. 6, pp. 1011–1029, 2021.

[9] S. J. Wang, Y. L. Sung, and J. X. Hong, "Sloped rolling-type bearings designed with linearly variable damping force," *Earthquakes and Structures*, vol. 19, no. 2, pp. 129–144, 2020.

[10] P. C. Chen, S. C. Hsu, Y. J. Zhong, and S. J. Wang, "Real-time hybrid simulation of smart base-isolated raised floor systems for high-tech industry," *Smart Structures and Systems*, vol. 23, no. 1, pp. 91–106, 2019.

[11] P. C. Chen and S. J. Wang, "Improved control performance of sloped rolling-type isolation devices using embedded electromagnets," *Structural Control and Health Monitoring*, vol. 24, no. 1, p. e1853, 2016.

[12] T. Y. Hsu, P. S. Dai, and S. J. Wang, "Numerical study on smart sloped rolling-type seismic isolators integrated with early prediction of peak velocity," *Engineering Structures*, vol. 246, Article ID 113032, 2021.

[13] T. Y. Hsu, C. H. Huang, and S. J. Wang, "Early adjusting damping force for sloped rolling-type seismic isolators based on earthquake early warning information," *Earthquakes and Structures*, vol. 20, no. 1, pp. 39–53, 2021.

[14] M. C. Smith, "Synthesis of mechanical networks: the inerter," *IEEE Transactions on Automatic Control*, vol. 47, no. 10, pp. 1648–1662, 2002.

[15] H. Garrido, O. Curadelli, and D. Ambrosini, "Improvement of tuned mass damper by using rotational inertia through tuned viscous mass damper," *Engineering Structures*, vol. 56, pp. 2149–2153, 2013.

[16] J. S. Hwang, J. Kim, and Y. M. Kim, "Rotational inertia dampers with toggle bracing for vibration control of a building structure," *Engineering Structures*, vol. 29, no. 6, pp. 1201–1208, 2007.

[17] S. J. Swift, M. C. Smith, A. R. Glover, C. Papageorgiou, B. Gartner, and N. E. Houghton, "Design and modelling of a fluid inerter," *International Journal of Control*, vol. 86, no. 11, pp. 2035–2051, 2013.

[18] R. Ma, K. Bi, and H. Hao, "Inerter-based structural vibration control: a state-of-the-art review," *Engineering Structures*, vol. 243, Article ID 112655, 2021.

[19] N. Alujević, D. Čakmak, H. Wolf, and M. Jokić, "Passive and active vibration isolation systems using inerter," *Journal of Sound and Vibration*, vol. 418, pp. 163–183, 2018.

[20] Y. Hu, M. Z. Q. Chen, Z. Shu, and L. Huang, "Analysis and optimisation for inerter-based isolators via fixed-point theory and algebraic solution," *Journal of Sound and Vibration*, vol. 346, pp. 17–36, 2015.

[21] M. Saitoh, "On the performance of gyro-mass devices for displacement mitigation in base isolation systems," *Structural Control and Health Monitoring*, vol. 19, no. 2, pp. 246–259, 2012.

[22] H. C. Tsai, "The effect of tuned-mass dampers on the seismic response of base-isolated structures," *International Journal of Solids and Structures*, vol. 32, no. 8-9, pp. 1195–1210, 1995.

[23] Y. Zhang and W. D. Iwan, "Protecting base-isolated structures from near-field ground motion by tuned interaction damper," *Journal of Engineering Mechanics*, vol. 128, no. 3, pp. 287–295, 2002.

[24] T. Taniguchi, A. Der Kiureghian, and M. Melkumyan, "Effect of tuned mass damper on displacement demand of base-isolated structures," *Engineering Structures*, vol. 30, no. 12, pp. 3478–3488, 2008.

[25] P. Xiang and A. Nishitani, "Optimum design for more effective tuned mass damper system and its application to base-isolated buildings," *Structural Control and Health Monitoring*, vol. 21, no. 1, pp. 98–114, 2014.

[26] D. De Domenico and G. Ricciardi, "Earthquake-resilient design of base isolated buildings with TMD at basement: application to a case study," *Soil Dynamics and Earthquake Engineering*, vol. 113, pp. 503–521, 2018.

[27] D. De Domenico and G. Ricciardi, "An enhanced base isolation system equipped with optimal tuned mass damper inerter (TMDI)," *Earthquake Engineering & Structural Dynamics*, vol. 47, no. 5, pp. 1169–1192, 2018.

[28] D. D. Domenico and G. Ricciardi, "Optimal design and seismic performance of tuned mass damper inerter (TMDI) for structures with nonlinear base isolation systems," *Earthquake Engineering & Structural Dynamics*, vol. 47, no. 12, pp. 2539–2560, 2018.

[29] M. De Angelis, A. Giaralis, F. Petrini, and D. Pietrosanti, "Optimal tuning and assessment of inertial dampers with grounded inerter for vibration control of seismically excited base-isolated systems," *Engineering Structures*, vol. 196, Article ID 109250, 2019.

[30] A. Di Matteo, C. Masnata, and A. Pirrotta, "Simplified analytical solution for the optimal design of Tuned Mass Damper Inerter for base isolated structures," *Mechanical Systems and Signal Processing*, vol. 134, Article ID 106337, 2019.

[31] D. De Domenico, P. Deastra, G. Ricciardi, N. D. Sims, and D. J. Wagg, "Novel fluid inerter based tuned mass dampers for optimised structural control of base-isolated buildings," *Journal of the Franklin Institute*, vol. 356, no. 14, pp. 7626–7649, 2019.

[32] D. Pietrosanti, M. De Angelis, and A. Giaralis, "Experimental study and numerical modeling of nonlinear dynamic response of SDOF system equipped with tuned mass damper inerter (TMDI) tested on shaking table under harmonic excitation," *International Journal of Mechanical Sciences*, vol. 184, Article ID 105762, 2020.

[33] C. Masnata, C. Matteo Adam, and A. Pirrotta, "Assessment of the tuned mass damper inerter for seismic response control of base-isolated structures," *Structural Control and Health Monitoring*, vol. 28, p. e2665, 2021.

[34] Z. Zhao, R. Zhang, Y. Jiang, and C. Pan, "Seismic response mitigation of structures with a friction pendulum inerter system," *Engineering Structures*, vol. 193, no. 15, pp. 110–120, 2019.

[35] F. Qian, Y. Luo, H. Sun, W. C. Tai, and L. Zuo, "Optimal tuned inerter dampers for performance enhancement of vibration isolation," *Engineering Structures*, vol. 198, no. 1, Article ID 109464, 2019.

[36] H. Sun, L. Zuo, X. Wang, J. Peng, and W. Wang, "Exact H_2 optimal solutions to inerter-based isolation systems for building structures," *Structural Control and Health Monitoring*, vol. 26, no. 6, p. e2357, 2019.

[37] H. Wang, W. Shen, H. Zhu, W. Wei, F. Kong, and S. Zhu, "Performance enhancement of FPS-isolated buildings using an inerter-based damper: stochastic seismic analysis and optimization," *Mechanical Systems and Signal Processing*, vol. 177, Article ID 109237, 2022.

[38] C. Pan, J. Jiang, R. Zhang, and Y. Xia, "Closed-form design formulae for seismically isolated structure with a damping enhanced inerter system," *Structural Control and Health Monitoring*, vol. 28, no. 12, p. e2840, 2021.

[39] R. S. Jangid, "Optimum tuned inerter damper for base-isolated structures," *Journal of Vibration Engineering & Technologies*, vol. 9, no. 7, pp. 1483–1497, 2021.

[40] P. Nyangi and K. Ye, "Optimal design of dual isolated structure with supplemental tuned inerter damper based on performance requirements," *Soil Dynamics and Earthquake Engineering*, vol. 149, Article ID 106830, 2021.

[41] C. A. Morales, "Inerter-added transmissibility to control base displacement in isolated structures," *Engineering Structures*, vol. 251, Article ID 113564, 2022.

[42] A. Zhao, R. Zang, N. Wierschem, Y. Jiang, and C. Pan, "Displacement mitigation-oriented design and mechanism for inerter-based isolation system," *Journal of Vibration and Control*, vol. 27, no. 17-18, pp. 1–13, 2021.

[43] S. K. Shahi and J. W. Baker, "An efficient algorithm to identify strong-velocity pulses in multicomponent ground motions," *Bulletin of the Seismological Society of America*, vol. 104, no. 5, pp. 2456–2466, 2014.